

---

Masters Theses

Student Theses and Dissertations

---

Spring 2014

## Numerical analysis of thermal stress and deformation in multi-layer laser metal deposition process

Heng Liu

Follow this and additional works at: [https://scholarsmine.mst.edu/masters\\_theses](https://scholarsmine.mst.edu/masters_theses)



Part of the [Manufacturing Commons](#)

Department:

---

### Recommended Citation

Liu, Heng, "Numerical analysis of thermal stress and deformation in multi-layer laser metal deposition process" (2014). *Masters Theses*. 7242.

[https://scholarsmine.mst.edu/masters\\_theses/7242](https://scholarsmine.mst.edu/masters_theses/7242)

This thesis is brought to you by Scholars' Mine, a service of the Missouri S&T Library and Learning Resources. This work is protected by U. S. Copyright Law. Unauthorized use including reproduction for redistribution requires the permission of the copyright holder. For more information, please contact [scholarsmine@mst.edu](mailto:scholarsmine@mst.edu).



NUMERICAL ANALYSIS OF THERMAL STRESS AND DEFORMATION IN  
MULTI-LAYER LASER METAL DEPOSITION PROCESS

by

HENG LIU

A THESIS

Presented to the Faculty of the Graduate School of the  
MISSOURI UNIVERSITY OF SCIENCE AND TECHNOLOGY

In Partial Fulfillment of the Requirements for the Degree

MASTER OF SCIENCE IN MANUFACTURING ENGINEERING

2014

Approved by

Frank Liou, Advisor  
K. Chandrashekhara  
Joseph W. Newkirk

© 2014  
Heng Liu  
All Rights Reserved

## ABSTRACT

Direct metal deposition (DMD) has gained increasing attention in the area of rapid manufacturing and repair. It has demonstrated the ability to produce fully dense metal parts with complex internal structures that could not be achieved by traditional manufacturing methods. However, this process involves extremely high thermal gradients and heating and cooling rates, resulting in residual stresses and distortion, which may greatly affect the product integrity. The purpose of this thesis is to study the features of thermal stress and deformation involved in the DMD process. Utilizing commercial finite element analysis (FEA) software ABAQUS, a 3-D, sequentially coupled, thermo-mechanical model was firstly developed to predict both the thermal and mechanical behavior of the DMD process of Stainless Steel 304. The simulation results show that the temperature gradient along height and length direction can reach 483 K/mm and 1416 K/mm, respectively. The cooling rate of one particular point can be as high as 3000 K/s. After the work piece is cooled down, large tensile stresses are found within the deposited materials and unrecoverable deformation exists. A set of experiments then were conducted to validate the mechanical effects using a laser displacement sensor. Comparisons between the simulated and experimental results show good agreement. The FEA code for this model can be used to predict the mechanical behavior of products fabricated by the DMD process and to help with the optimization of design and manufacturing parameters.

## ACKNOWLEDGMENTS

There are some people whom I would like to thank greatly in helping me through the research work and writing this thesis. I would like to thank my advisor, Dr. Frank Liou, for the chance to be a member of an inspiring research group, for the opportunity to work on interesting and challenging projects, for his generous financial support through my graduate career, and his continuous advice, perseverance and guidance in helping me keep motivated. I would like to thank the other members of my thesis committee, Dr. Joseph W. Newkirk and Dr. K. Chandrashekhara for their insightful comments and assistance in the research process.

I would also like to thank Todd Sparks for his valuable support in sharing ideas with me and conducting the experiments. I am also grateful to the following former or current students in LAMP lab for their various forms of support during my graduate study—Xueyang Chen, Nanda Dey, Dr. Zhiqiang Fan, Sreekar Karnati, Renwei Liu, Niroop Matta, Zhiyuan Wang, Jingwei Zhang, Yunlu Zhang.

I am also thankful to the academic and financial support from the Department of Mechanical and Aerospace Engineering and Manufacturing program.

Last but not least, I would like to give my grateful acknowledge to my parents, for the immeasurable care, support and love they give me since the first day I was born.

## TABLE OF CONTENTS

	Page
ABSTRACT .....	iii
ACKNOWLEDGMENTS .....	iv
LIST OF ILLUSTRATIONS .....	vii
LIST OF TABLES .....	viii
NOMENCLATURE .....	ix
SECTION	
1. INTRODUCTION .....	1
1.1. LASER AIDED DIRECT METAL DEPOSITION .....	1
1.2. RESIDUAL STRESS AND DISTORTION .....	1
1.3. LITERATURE REVIEW .....	2
1.4. SIMULATION AND EXPERIMENT APPROACH .....	4
2. THERMAL ANALYSIS .....	6
2.1. GOVERNING EQUATIONS .....	6
2.2. INITIAL AND BOUNDARY CONDITIONS .....	6
2.3. ADJUSTMENTS AND ASSUMPTIONS .....	7
2.3.1. Energy Distribution of the Laser Beam .....	7
2.3.2. Movement of Laser Beam .....	7
2.3.3. Powder Addition .....	7
2.3.4. Latent Heat of Fusion .....	8
2.3.5. Marangoni Effect .....	8
2.3.6. Combined Boundary Conditions .....	9
2.4. FINITE ELEMENT MODELING .....	9
2.4.1. Dimension and Parameter .....	9
2.4.2. Material Properties .....	10
2.4.3. Element Selection .....	10
2.4.4. Increment Control .....	12
3. MECHANICAL ANALYSIS .....	13
3.1. GOVERNING EQUATIONS .....	13

3.2. INITIAL AND BOUNDARY CONDITIONS .....	14
3.3. FINITE ELEMENT MODELING .....	15
3.3.1. Material Properties .....	15
3.3.2. Element Selection.....	15
4. NUMERICAL RESULTS AND EXPERIMENTAL VALIDATION.....	16
4.1. TEMPERATURE .....	16
4.1.1. Temperature Field .....	16
4.1.2. Temperature Gradient.....	21
4.1.3. Heating and Cooling Rate .....	22
4.1.4. Superheat .....	23
4.2. INSTANTANEOUS STRESS .....	24
4.3. RESIDUAL STRESS.....	25
4.4. DEFORMATION .....	31
4.4.1. Experiment Setup .....	32
4.4.2. Experimental and Simulation Results .....	33
5. DISCUSSION .....	36
6. CONCLUSION AND SCOPE OF FUTURE WORK .....	38
6.1. CONCLUDING REMARKS.....	38
6.2. SCOPE OF FUTURE WORK .....	38
APPENDICES	
A. SUBROUTINE TO SIMULATE THE MOVING HEAT SOURCE.....	40
B. SUBROUTINE TO SIMULATE THE COMBINED BOUNDARY CONDITION.....	43
C. TEMPERATURE-DEPENDNET THERMAL PROPERTIES OF AISI 304 STAINLESS STEEL.....	45
D. TEMPERATURE-DEPENDNET MECHANICAL PROPERTIES OF AISI 304 STAINLESS STEEL.....	47
BIBLIOGRAPHY.....	51
VITA.....	54



## LIST OF ILLUSTRATIONS

	Page
Figure 1.1. Flow Chart Showing the Process of Numerical Modeling.....	4
Figure 2.1. Dimension of DMD specimen.....	10
Figure 2.2. Meshing Scheme .....	11
Figure 3.1. Elements Used in Thermal and Mechanical Analysis .....	15
Figure 4.1. Contour Plots of Temperature Field of the Melt pool and Surrounding Areas from Top View at Different Times (Case 1).....	16
Figure 4.2. Contour Plots of Temperature Field and Isotherms of the Substrate and Deposits from Side View at Different Times (Case 1).....	17
Figure 4.3. Contour Plots of Temperature Field of the Melt pool and Surrounding Areas from Top View at Different Times (Case 2).....	19
Figure 4.4. Contour Plots of Temperature Field and Isotherms of the Substrate and Deposits from Side View at Different Times (Case 2).....	20
Figure 4.5. Location of Points within Deposition Under Consideration .....	22
Figure 4.6. Temperature of Nodes in x and y Directions in Case 1 at $t = 4.5$ s.....	22
Figure 4.7. Temperature History of Nodes a, b, and c.....	23
Figure 4.8. Superheating Temperature in Each Deposition Layer in Case 1.....	24
Figure 4.9. Instantaneous von Mises Stress during the DMD Process .....	25
Figure 4.10. Contour Plots of Residual Stress Field within Deposits (exterior faces) .....	26
Figure 4.11. Contour Plots of Residual Stress Field within Deposits (y-y cross section)	27
Figure 4.12. Residual Stress at the Top Surface of Deposits.....	28
Figure 4.13. Residual Stress at the Bottom Surface of Deposits .....	30
Figure 4.14. Final Shape of Substrate.....	32
Figure 4.15. Deflection of Substrate along y .....	32
Figure 4.16. Experimental Setup .....	33
Figure 4.17. Laser Displacement Sensor .....	33
Figure 4.18. Simulation and Experimental Results of Substrate Deflection .....	34

**LIST OF TABLES**

	Page
Table 2.1. Latent Heat of Fusion for Stainless Steel 304.....	8
Table 2.2. DMD Process Parameters .....	10

## NOMENCLATURE

Symbol	Description
$T$	Temperature
$\rho$	Density of the material
$C$	Heat conductivity
$k$	Density of the material
$Q$	Internal heat generation per unit volume
$T_0$	Ambient temperature
$\mathbf{n}$	Normal vector of the surface
$h_c$	Heat convection coefficient
$\varepsilon$	Emissivity
$\sigma$	Stefan-Boltzman constant
$\Gamma$	Surfaces of the work piece
$\Lambda$	Surface area irradiated by the laser beam
$\alpha$	Absorption coefficient
$P$	Laser power
$r$	Radius of the laser beam
$R$	Position of the laser beam's center
$u$	Velocity the laser beam travels along x direction
$v$	Velocity the laser beam travels along y direction
$w$	Velocity the laser beam travels along z direction
$c_p^*$	Equivalent specific heat
$c_p$	Specific heat
$L$	Latent heat of fusion
$T_m$	Melting temperature
$k_m$	Modified thermal conductivity
$T_{liq}$	Liquidus temperature
$h$	Combined heat transfer coefficient

$\Delta t$	Time increment
$\Delta l$	Typical element dimension
$\varepsilon_{ij}$	Total strain
$\varepsilon_{ij}^M$	Strain from the mechanical forces
$\varepsilon_{ij}^T$	Strain from thermal loads
$\varepsilon_{ij}^E$	Elastic strain
$\varepsilon_{ij}^P$	Plastic strain
$\varepsilon_{ij}^T$	Thermal strain
$\varepsilon_{ij}^{\Delta V}$	Strain due to the volumetric change
$\varepsilon_{ij}^{Tp}$	Strain caused by transformation plasticity
$D_{ijkl}$	Elastic stiffness tensor
$E$	Young's modulus
$\nu$	Poisson's ratio
$\delta_{ij}$	Kronecker delta function
$d\varepsilon_{ij}^P$	Plastic strain increment
$\lambda$	Plastic multiplier
$s_{ij}$	Deviatoric stress tensor

# **1. INTRODUCTION**

## **1.1. LASER AIDED DIRECT METAL DEPOSITION**

Laser aided direct metal deposition (DMD) is an advanced additive manufacturing (AM) technology which can produce fully dense, functional metal parts directly from CAD model. In its operation, laser beam is focused onto a metallic substrate to create a melt pool and a powder stream is continuously conveyed into the melt pool by the powder delivery system. The substrate is attached to a computer numerical control (CNC) multi-axis system, and by moving the substrate according to a desired route pattern, a 2-D layer can be deposited. By building successive layers on top of one another (layer by layer), a 3-D object can be formed. The DMD process has demonstrated its ability in the area of rapid manufacture, repair, and modification of metallic components. Practically, this process is most suitable for components with complex internal geometries which cannot be fabricated by traditional manufacturing methods such as casting. Furthermore, this process is very cost effective compared with traditional subtractive manufacturing techniques because it can produce near-net shape parts with little or no machining (Liou & Kinsella, 2009).

## **1.2. RESIDUAL STRESS AND DISTORTION**

Residual stresses are those stresses that would exist in a body if all external loads were removed. When a material is heated uniformly, it expands uniformly and no thermal stress is produced. But when the material is heated unevenly, thermal stress is produced (Masubuchi, 1980).

Highly localized heating and cooling during the DMD process produces non-uniform thermal expansion and contraction, which results in a complicated distribution of residual stresses in the heat affect zone and unexpected distortion across the entire structure. The residual stresses may promote fractures and fatigue and induce unpredictable buckling during the service of deposited parts. This distortion often is detrimental to the dimensional accuracies of structures; therefore, it is vital to predict the

behavior of materials after the DMD process and to optimize the design/manufacturing parameters in order to control the residual stresses and distortion.

### **1.3. LITERATURE REVIEW**

The thermal behavior of the DMD process has been investigated numerically by many scholars. Kim and Peng (2000) built a 2-D finite element model to simulate the temperature field during the laser cladding process. The results indicated that quasi-steady thermal field cannot be reached in a short time. Other scholars have chosen to experimentally investigate thermal behavior. Griffith et al. (1999) employed radiation pyrometers and thermocouples to monitor the thermal signature during laser engineered net shaping (LENS) processing. The results showed that the integrated temperature reheat had a significant effect on the microstructural evolution during fabrication of hollow H13 tool steel parts. Utilizing a two-wavelength imaging pyrometer, Wang et al. (2007) measured the temperature distribution in the melt pool and the area surrounding it during the LENS deposition process. It was found that the maximum temperature in the molten pool is approximately 1600 °C. Only thermal behaviors were investigated in these papers while no residual stresses were modeled and analyzed.

Some researchers have focused on the modeling and simulation of traditional welding processes, which share many similarities with DMD processes. Using a double-ellipsoid heat source, Gery et al. (2005) generated the transient temperature distributions of the welded plates. The results demonstrated that the welding speed, energy input and heat source distributions had important effects on the shape and boundaries of heat affect zone (HAZ). Deng (2009) investigated the effects of solid-state phase transformation on the residual stress and distortion caused by welding in low carbon and medium steels. The simulation results revealed that the final residual stress and the welding distortion in low carbon steel do not seem to be influenced by the solid-state phase transformation. However, for the medium carbon steel, the final residual stresses and the welding distortion seem to be significantly affected by the martensitic transformation. Feli et al. (2012) analyzed the temperature history and the residual stress field in multi-pass, butt-welded, stainless steel pipes. It was found that in the weld zone and its vicinity, a tensile axial

residual stress is produced on the inside surface, and compressive axial stress at outside surface.

Other researchers have attempted to obtain the distribution of residual stress caused by the DMD process through experiments. For example, Moat et al. (2011) measured strain in three directions using a neutron diffraction beam line to calculate the stress in DMD manufactured Waspaloy blocks. They found that large tensile residual stresses exist in the longitudinal direction near the top of the structure. Zheng et al. (2004) measured residual stress in PZT thin films fabricated by a pulsed laser using X-ray diffraction. Although experiments can provide relatively accurate results, their flexibility and high cost limit their ability to serve as a general method by which to solve residual stress problems.

In recent years, analyses of the residual stress involved in laser deposition processes using the FE model have been well documented in the literary. Aggarangsi et al. (2003) built a 2-D FE model to observe the impact of process parameters on the melt pool size, growth-direction residual stress and material properties in laser-based deposition processes. They observed that after deposition was completed and the wall was cooled to room temperature, large tensile stresses exist in the vertical direction at vertical free edges, which is contrast to the observations in this study. Wang et al. (2008) utilized commercial welding software SYSWELD to characterize the residual stress in LENS-deposited AISI 410 stainless steel thin wall plates. Tensile longitudinal stresses were found near the mid-height and compressive stresses were found near the top and bottom of the walls. Kamara et al. (2011) investigated the residual stress characteristics of laser deposited, multiple-layer wall of Waspaloy on an Inconel 718 substrate. The results indicated that along the length of the wall, residual stresses were almost zero at the bottom and top of the wall. Along the height of the wall, tensile stress with large magnitudes existed at the bottom of the wall while close to the top surface, near stress-free condition seem to prevail. This matches well with the results presented in this thesis.

#### 1.4. SIMULATION AND EXPERIMENT APPROACH

Based on the finite element (FE) analysis package ABAQUS, a 3-D, sequentially coupled, thermo-mechanical model was developed to simulate the transient temperature field, residual stress and final deformation involved in the DMD process of Stainless Steel 304 (SS 304). The numerical modeling involved two main steps and the solution processes are shown in Figure 1.1. In the first step, a transient thermal analysis was carried out to generate the temperature history of the entire work piece. In the second step, mechanical analysis was conducted to calculate the residual stress and deformation of work piece, and the load for this step is the temperature field file generated in previous step.

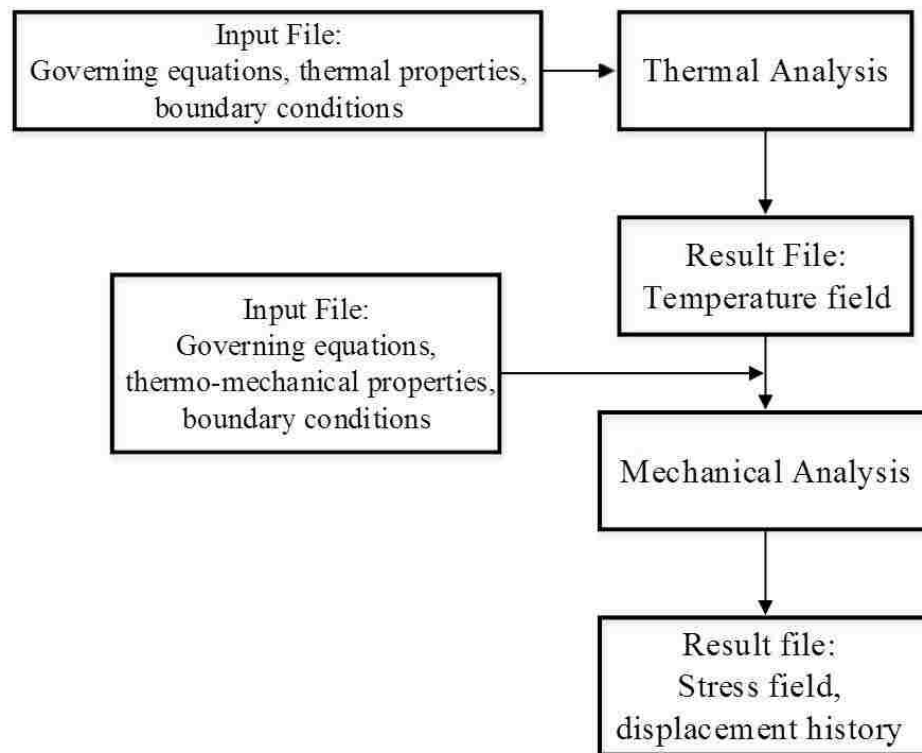


Figure 1.1. Flow Chart Showing the Process of Numerical Modeling

The experiment was conducted by using a laser displacement sensor to record the deflection of the substrate caused by thermal stresses during the deposition process. By



comparing the experimental results with simulation results, the numerical model was validated. This validated model can be extended to multi-layer laser aided DMD process of Stainless Steel under various process parameters and further to other materials.

## 2. THERMAL ANALYSIS

### 2.1. GOVERNING EQUATIONS

In the DMD process, the stress/deformation field in a structure would largely depend on the temperature field, but the influence of the stress/deformation field on the temperature field is negligible. Thus, a heat transfer analysis not coupled with mechanical effect is considered.

The transient temperature field  $T(x, y, z, t)$  throughout the domain was obtained by solving the 3-D heat conduction equation, Eq. (1), in the substrate, along with the appropriate initial and boundary conditions (Reddy, 2010).

$$\rho C \frac{\partial T}{\partial t} = \frac{\partial}{\partial x} \left( k \frac{\partial T}{\partial x} \right) + \frac{\partial}{\partial y} \left( k \frac{\partial T}{\partial y} \right) + \frac{\partial}{\partial z} \left( k \frac{\partial T}{\partial z} \right) + Q \quad (1)$$

where  $T$  is the temperature,  $\rho$  is the density,  $C$  is the specific heat,  $k$  is the heat conductivity, and  $Q$  is the internal heat generation per unit volume. All material properties were considered temperature-dependent.

### 2.2. INITIAL AND BOUNDARY CONDITIONS

The initial conditions applied to solve Eq. (1) were:

$$T(x, y, z, 0) = T_0 \quad (2)$$

$$T(x, y, z, \infty) = T_0 \quad (3)$$

where  $T_0$  is the ambient temperature. In this study,  $T_0$  was set as room temperature, 298 K. The boundary conditions including thermal convection and radiation, are described by Newton's law of cooling and the Stefan-Boltzmann law, respectively. The internal heat source term,  $Q$  in Eq. (1), also was considered in the boundary conditions as a surface heat source (moving laser beam). The boundary conditions then could be expressed as (Reddy, 2010):

$$K(\Delta T \cdot \mathbf{n})|_{\Gamma} = \begin{cases} \left[ -h_c(T - T_0) - \varepsilon\sigma(T^4 - T_0^4) \right] |_{\Gamma} & \Gamma \notin \Lambda \\ \left[ Q - h_c(T - T_0) - \varepsilon\sigma(T^4 - T_0^4) \right] |_{\Gamma} & \Gamma \in \Lambda \end{cases} \quad (4)$$

where  $k$ ,  $T$ ,  $T_0$  and  $Q$  bear their previous definitions,  $\mathbf{n}$  is the normal vector of the surface,  $h_c$  is the heat convection coefficient,  $\varepsilon$  is the emissivity which is 0.9,  $\sigma$  is the Stefan-Boltzman constant which is  $5.6704 \times 10^{-8} \text{ W/m}^2\text{K}^4$ ,  $\Gamma$  represents the surfaces of the work piece and  $\Lambda$  represents the surface area irradiated by the laser beam.

### 2.3. ADJUSTMENTS AND ASSUMPTIONS

Accurate modeling of the thermal process results in highly nonlinear coupled equations. To simplify the solution process and reduce the computational cost, the following adjustments and assumptions were considered.

**2.3.1. Energy Distribution of the Laser Beam.** In the experiment, a circular shaped laser beam shot onto the substrate vertically with a constant and uniform power density. Thus, the heat source term  $Q$  in Eq. (1) was considered a constant and uniformly distributed surface heat flux defined as:

$$Q = \frac{\alpha P}{\pi r^2} \quad (5)$$

where  $\alpha$  is the absorption coefficient,  $P$  is the power of the continuous laser, and  $r$  is the radius of the laser beam.  $\alpha$  was set as 0.4 according to numerous experimental conducted in LAMP lab at Missouri S&T, and  $r = 1.25 \text{ mm}$ .

**2.3.2. Movement of Laser Beam.** The motion of the laser beam was taken into account by updating the position of the beam's center  $R$  with time  $t$  as follows:

$$R = \left[ \left( x - \int_{t_0}^t u dt \right) + \left( y - \int_{t_0}^t v dt \right) + \left( z - \int_{t_0}^t w dt \right) \right]^{\frac{1}{2}} \quad (6)$$

where  $x$ ,  $y$ , and  $z$  are the spatial coordinate the laser beam center,  $u$ ,  $v$ , and  $w$  are the continuous velocities the laser beam travels along  $x$ ,  $y$ , and  $z$  direction.

In ABAQUS, a user subroutine "DFLUX" (Simulia, 2011) was written to simulate the motion of the laser beam (Appendix A).

**2.3.3. Powder Addition.** In modeling, the continuous powder addition process is divided into many small time steps. Using the "Model Change" (Simulia, 2011), in each time step, a set of elements was added onto the substrate to form rectangular deposits

along the centerline of the substrate. The width of the deposits was assumed to be the same as the diameter of the laser beam, and the thickness of the deposits was calculated from the speed at which the laser traveled and the powder feed rate with an efficiency of 0.3. The geometry of the deposits was updated at the end of each step to simulate corresponding boundary conditions.

**2.3.4. Latent Heat of Fusion.** The effect of the latent heat of fusion during the melting/solidification process was accounted for by modifying the specific heat. The equivalent specific heat  $c_p^*$  is expressed as (Toyserkani et al., 2004):

$$c_p^*(T) = c_p(T) + \frac{L}{T_m - T_0} \quad (6)$$

where  $c_p^*(T)$  is the modified specific heat,  $c_p(T)$  is the original temperature-dependent specific heat,  $L$  is the latent heat of fusion,  $T_m$  is the melting temperature, and  $T_0$  is the ambient temperature. The values of the latent heat of fusion, solidus temperature and liquidus temperature of SS 304 (Ghosh, 2006) appear in Table 2.1.

Table 2.1. Latent Heat of Fusion for Stainless Steel 304

Latent Heat of Fusion (J/kg)	Solidus Temperature (K)	Liquidus Temperature (K)
273790	1703	1733

**2.3.5. Marangoni Effect.** The effect of Marangoni flow caused by the thermocapillary phenomenon significantly impacts the temperature distribution so it must be considered in order to obtain an accurate thermal field solution (Alimardani et al., 2007). Based on the method proposed by Lampa et al. (Lampa et al., 1997), artificial thermal conductivity was used to account for the Marangoni effect:

$$k_m(T) = \begin{cases} k(T) & T \leq T_{liq} \\ 2.5 \cdot k(T) & T > T_{liq} \end{cases} \quad (7)$$

where  $k_m(T)$  is the modified thermal conductivity,  $T_{liq}$  is the liquidus temperature, and  $T$  and  $k(T)$  maintain their previous definitions.

**2.3.6. Combined Boundary Conditions.** The boundary conditions shown in Eq. 4 can be rewritten as:

$$K(\Delta T \cdot \mathbf{n})|_{\Gamma} = \begin{cases} [(-h_c - h_r)(T - T_0)]|_{\Gamma} & \Gamma \notin \Lambda \\ [Q - (-h_c - h_r)(T - T_0)]|_{\Gamma} & \Gamma \in \Lambda \end{cases} \quad (8)$$

where  $h_r$  is the radiation coefficient expressed as:

$$h_r = \varepsilon\sigma(T^2 + T_0^2)(T + T_0) \quad (9)$$

Eq. (8) indicates that convection was dominant at low temperatures, while radiation made a major contribution to heat loss at high temperatures. Because Eq. (9) is a 3rd-order function of temperature  $T$ , a highly nonlinear term was introduced by the radiation coefficient, thus greatly increasing the computational expense. Based on experimental data, an empirical formula combining convective and radiative heat transfer was given by Vinokurov (1977) as:

$$h = h_c + \varepsilon\sigma(T^2 + T_0^2)(T + T_0) \approx 2.41 \times 10^{-3} \varepsilon T^{1.61} \quad (10)$$

where  $h$  is the combined heat transfer coefficient which is a lower order function of temperature  $T$  compared with  $h_r$ . The associated loss in accuracy using this relationship is estimated to be less than 5% (Labudovic and Kovacevic, 2003). In ABAQUS, a user subroutine “FILM” is written to simulate heat loss (Appendix B).

## 2.4. FINITE ELEMENT MODELING

**2.4.1. Dimension and Parameter.** As shown in Figure. 2.1, a finite element model for a 1-pass, 3-layer DMD process was built. The dimension of substrate under consideration is  $50.8 \times 12.7 \times 3.175$  mm ( $2 \times 0.5 \times 0.125$  inch). Two cases were simulated with different process parameters including laser power, laser travel speed and powder feed rate. These parameters were chosen according to the criterion that the final geometry of deposits and the total energy absorbed by the specimen be the same in each case. These process parameters are detailed in Table 2.2.

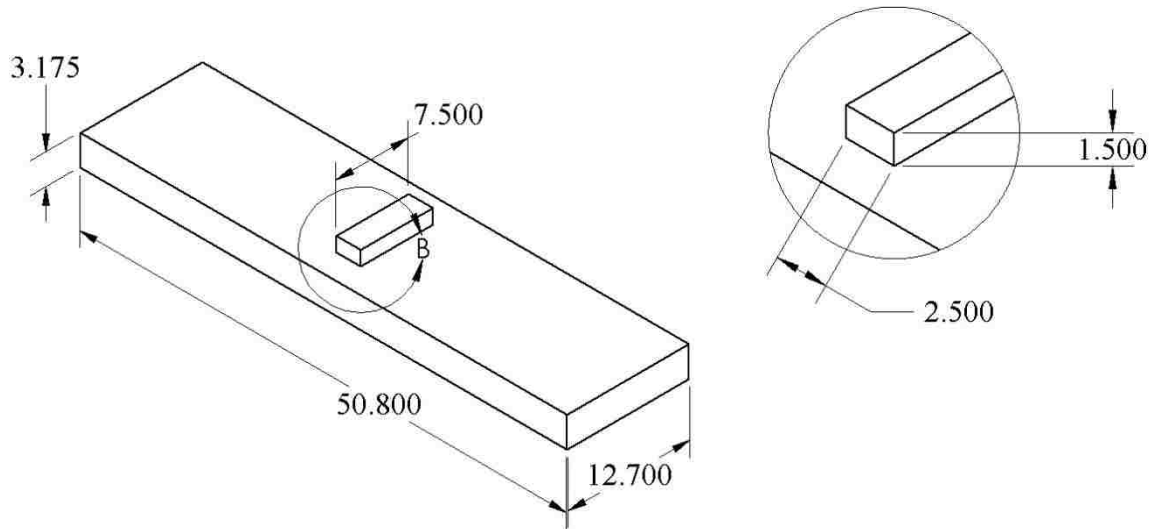


Figure 2.1. Dimension of DMD specimen

Table 2.2. DMD Process Parameters

Case Number	Laser Power (W)	Laser Travel Speed (mm/min)	Powder Feed Rate (g/min)
1	607	250	6.3
2	910	375	9.4

**2.4.2. Material Properties.** Temperature-dependent thermal physical properties of SS 304, including density, specific heat, thermal conductivity and latent heat, were used as inputs. The values of these properties appear in Appendix C.

**2.4.3. Element Selection.** The type and size of elements used to approximate the domain were determined on the basis of computational accuracy and cost. In transient heat transfer analysis with second-order elements, there is a minimum required time increment. A simple guideline is (Simulia, 2011):

$$\Delta t > \frac{6c}{\rho k} \Delta l^2 \quad (11)$$

where  $c$ ,  $\rho$  and  $k$  are as previously defined,  $\Delta t$  is the time increment, and  $\Delta l$  is a typical element dimension. If the time increment is smaller than this value, nonphysical

oscillations may appear in the solution. Such oscillations are eliminated with first-order elements (Simulia, 2011) but can lead to inaccurate solutions (Reddy, 2010). Considering the stability along with the computational time and accuracy, first-order 3-D heat transfer elements (C3D8) with h-version mesh refinement (refine the mesh by subdividing existing elements into more elements of the same order) were used for the whole domain. Fine meshes were used in the deposition zone, and the mesh size gradually increased with the distance from the deposits. In regions more separated from the heat affect zone, coarser meshes were utilized. As shown in Figure 2.2, 14496 elements and 17509 nodes were created.

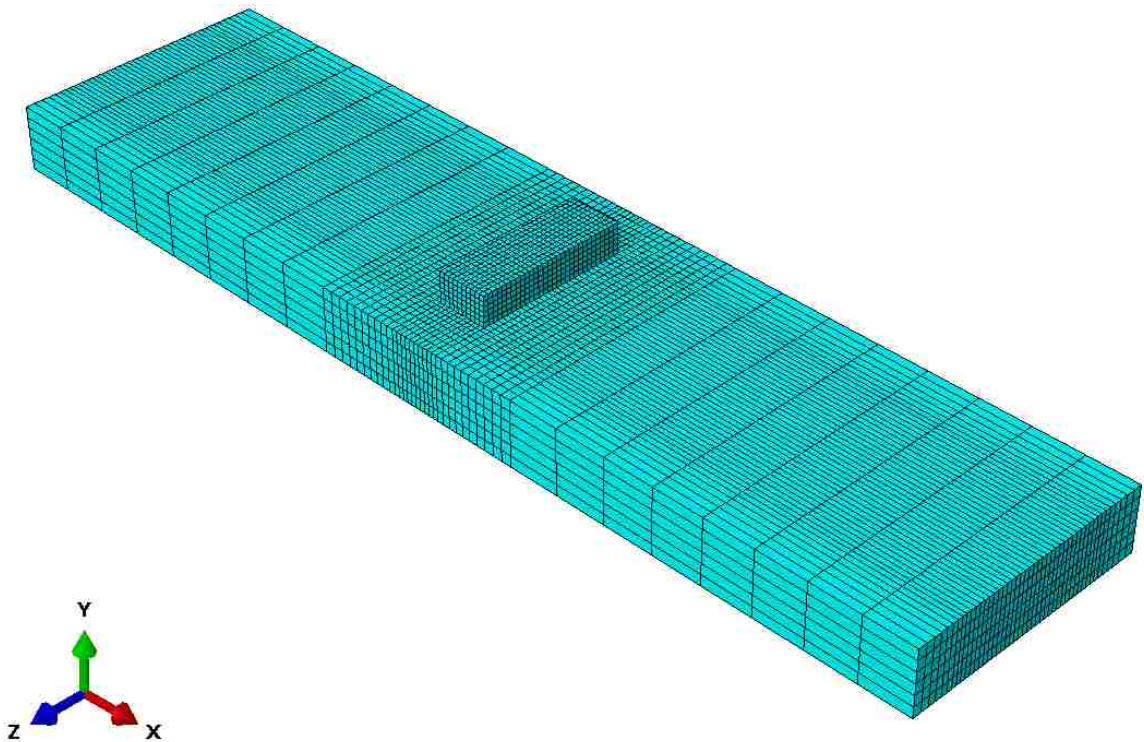


Figure 2.2. Meshing Scheme

**2.4.4. Increment Control.** In order to obtain reliable results from the mechanical analysis, the maximum nodal temperature change in each increment was set as  $5 K$  and the time increments were selected automatically by ABAQUS to ensure that this value was not exceeded at any node during any increment of the analysis (Simulia, 2011).



### 3. MECHANICAL ANALYSIS

#### 3.1. GOVERNING EQUATIONS

The total strain  $\varepsilon_{ij}$  can be represented generally as:

$$\varepsilon_{ij} = \varepsilon_{ij}^M + \varepsilon_{ij}^T \quad (12)$$

where  $\varepsilon_{ij}^M$  is the strain contributed by the mechanical forces and  $\varepsilon_{ij}^T$  is the strain from thermal loads. Eq. (12) can be decomposed further into five components as (Deng, 2009):

$$\varepsilon_{ij} = \varepsilon_{ij}^E + \varepsilon_{ij}^P + \varepsilon_{ij}^T + \varepsilon_{ij}^{\Delta V} + \varepsilon_{ij}^{Trp} \quad (13)$$

where  $\varepsilon_{ij}^E$  is the elastic strain,  $\varepsilon_{ij}^P$  is the plastic strain,  $\varepsilon_{ij}^T$  is the thermal strain,  $\varepsilon_{ij}^{\Delta V}$  is the strain due to the volumetric change in the phase transformation and  $\varepsilon_{ij}^{Trp}$  is the strain caused by transformation plasticity. Solid-state phase transformation does not exist in stainless steel (Deng and Murakawa, 2006), so  $\varepsilon_{ij}^{\Delta V}$  and  $\varepsilon_{ij}^{Trp}$  vanish. The total strain vector is then represented as:

$$\varepsilon_{ij} = \varepsilon_{ij}^E + \varepsilon_{ij}^P + \varepsilon_{ij}^T \quad (14)$$

The elastic stress-strain relationship is governed by isotropic Hooke's law as:

$$\sigma_{ij} = D_{ijkl} \varepsilon_{ij}^E \quad (i, j, k, l = 1, 2, 3) \quad (15)$$

where  $D_{ijkl}$  is the elastic stiffness tensor calculated from Young's modulus  $E$  and Poisson's ratio  $\nu$  as (Kamara et al., 2011):

$$D_{ijkl} = \frac{E}{1+\nu} \left[ \frac{1}{2} (\delta_{ik} \delta_{jl} + \delta_{ij} \delta_{kl}) + \frac{\nu}{1-2\nu} \delta_{ij} \delta_{kl} \right] \quad (16)$$

where  $\delta_{ij}$  is the Kronecker delta function defined as:

$$\delta_{ij} = \begin{cases} 1 & \text{for } i = j \\ 0 & \text{for } i \neq j \end{cases} \quad (17)$$

For isotropic elastic solids, Eq. (15) can be simplified as:

$$\varepsilon_{ij}^E = \frac{1+\nu}{E} \sigma_{ij} - \frac{\nu}{E} \sigma_{kk} \delta_{ij} \quad (18)$$

Thermal strain  $\varepsilon_{ij}^T$  can be calculated from the thermal expansion constitutive equation:

$$\varepsilon_{ij}^T = \alpha \Delta T \delta_{ij} \quad (19)$$

where  $\alpha$  is the thermal expansion coefficient, and  $\Delta T$  is the temperature difference between two different material points. Rate-independent plasticity with the von Mises yield criterion and linear kinematic hardening rule (Deng and Murakawa, 2006) were utilized to model the plastic strain.

Unlike the elastic and thermal strain, no unique relationship exists between the total plastic strain and stress; when a material is subjected to a certain stress state, there exist many possible strain states. So strain increments, instead of the total accumulated strain, were considered when examining the strain-stress relationships. The total strain then was obtained by integrating the strain increments over time  $t$ . The plastic strain-stress relationship for isotropic material is governed by the Prandtl-Reuss equation (Chakrabarty, 2006):

$$d\varepsilon_{ij}^P = \lambda s_{ij} \quad (20)$$

where  $d\varepsilon_{ij}^P$  is the plastic strain increment,  $\lambda$  is the plastic multiplier, and  $s_{ij}$  is the deviatoric stress tensor defined by:

$$s_{ij} = \sigma_{ij} - \frac{1}{3} \sigma_{kk} \delta_{ij} \quad (21)$$

By substituting Eq. (18), Eq. (19), Eq. (20) and Eq. (21) into Eq. (14) and taking the derivative with respect to time, the total strain rate can be described by (Zhu and Chao, 2002):

$$\dot{\varepsilon}_{ij} = \frac{1+\nu}{E} \dot{\sigma}_{ij} - \frac{\nu}{E} \dot{\sigma}_{kk} \delta_{ij} + \alpha \dot{T} \delta_{ij} + \lambda \left( \sigma_{ij} - \frac{1}{3} \sigma_{kk} \delta_{ij} \right) \quad (22)$$

### 3.2. INITIAL AND BOUNDARY CONDITIONS

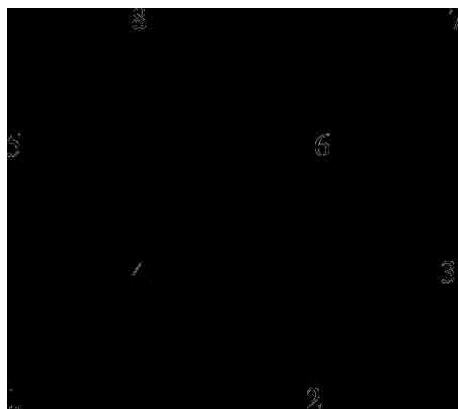
The temperature history of all the nodes generated in the thermal analysis was imported as a predefined field into the mechanical analysis. The only boundary condition applied to the domain was that the substrate was fixed on one side to prevent rigid body motion. In ABAQUS, the node displacements on the left side of the substrate were set as 0.

### 3.3. FINITE ELEMENT MODELING

**3.3.1. Material Properties.** Temperature-dependent mechanical properties including the thermal expansion coefficient (Kim, 1975), Young’s modulus, Poisson’s ratio (Deng and Murakawa, 2006) and yield stress (Ghosh, 2006) were used to model the thermo-mechanical behavior of SS 304 . The values of these properties appear in Appendix D.

**3.3.2. Element Selection.** The order of element and integration method used in the mechanical analysis differed from those used in the thermal analysis, while the element dimension and meshing scheme remained unchanged. To ensure the computational accuracy of the residual stress and deformation, second- order elements were utilized in the heat affection zone while first-order elements were used in other regions to reduce the computation time. Prevent shear and volumetric locking (Simulia, 2011) requires the selection of reduced-integration elements. Therefore, elements “C3D20R” and “C3D8R” in ABAQUS were combined in use to represent the domain.

As shown in Fig. 3.1, the 3-D 20-node element used in the mechanical analysis had 12 more nodes than the 3-D 8-node element used in the thermal analysis. Therefore, when mapping the temperature data from the thermal analysis to the mechanical analysis, interpolation had to be conducted to obtain the temperature of the 12 extra mid-side nodes (Nodes 9–20 in Figure 3.1(b)).



(a) 8-node brick element



(b) 20-node brick element

Figure 3.1. Elements Used in Thermal and Mechanical Analysis

## 4. NUMERICAL RESULTS AND EXPERIMENTAL VALIDATION

### 4.1. TEMPERATURE

**4.1.1. Temperature Field.** Figure 4.1 shows the temperature field of the melt pool and surrounding areas from top view at different times in Case 1 (laser power 607 W, laser travel speed 250 mm/min, powder feed rate 6.3 g/min). Figure 4.2 shows the temperature field and isotherms of the substrate and deposits from side view at different times in Case 1. The peak temperature during the process was around 2350 K, while the lowest temperature was close to room temperature. The big temperature differences and small geometrical dimensions caused very large temperature gradients.

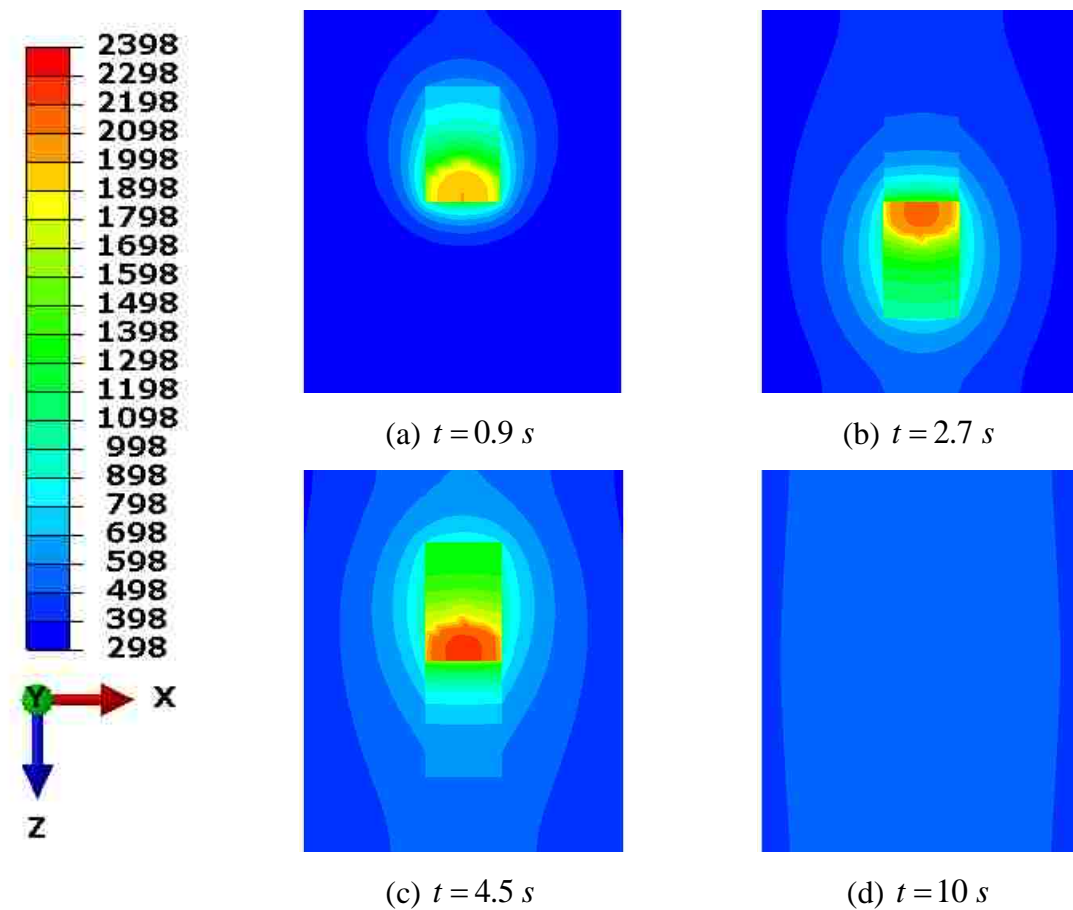


Figure 4.1. Contour Plots of Temperature Field of the Melt pool and Surrounding Areas from Top View at Different Times (Case 1)

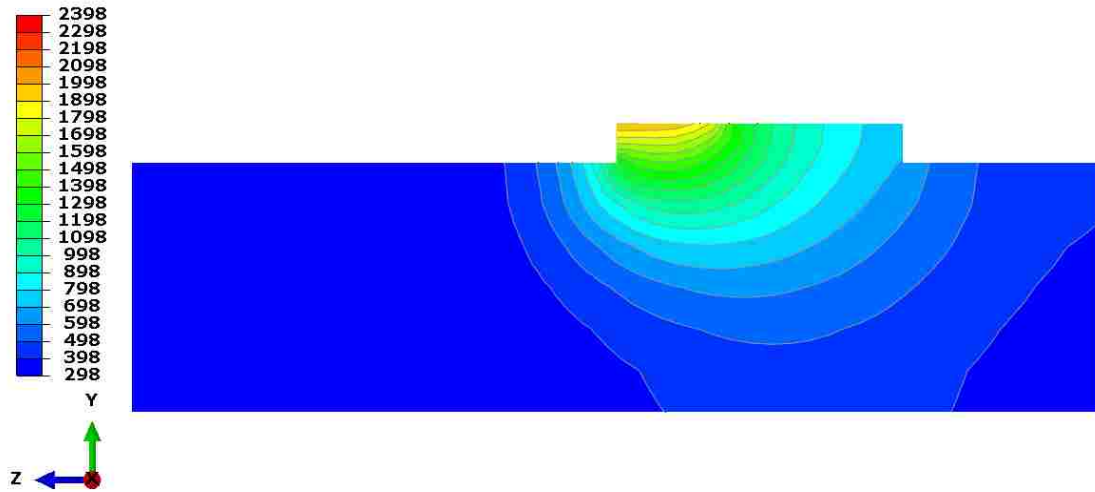
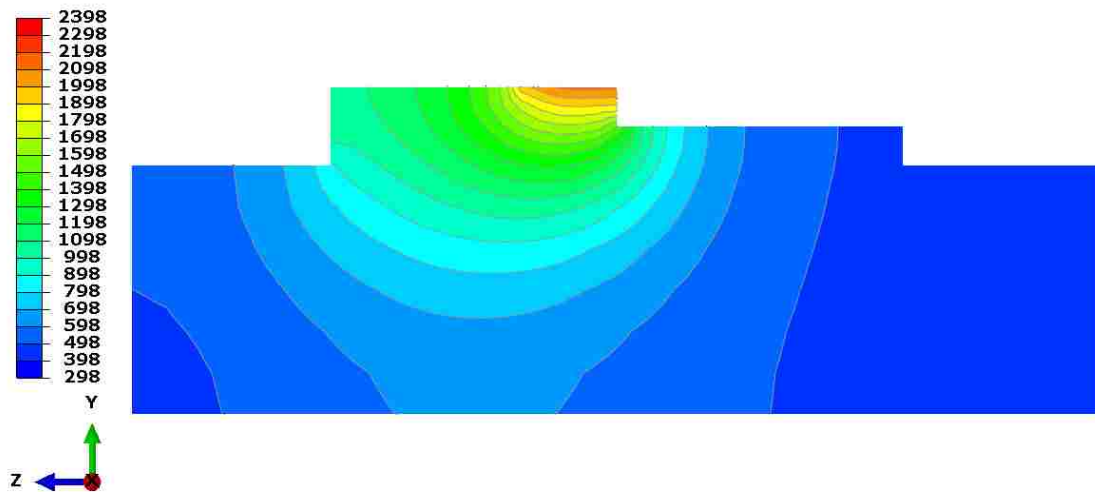
(a)  $t = 0.9$  s(b)  $t = 2.7$  s

Figure 4.2. Contour Plots of Temperature Field and Isotherms of the Substrate and Deposits from Side View at Different Times (Case 1)

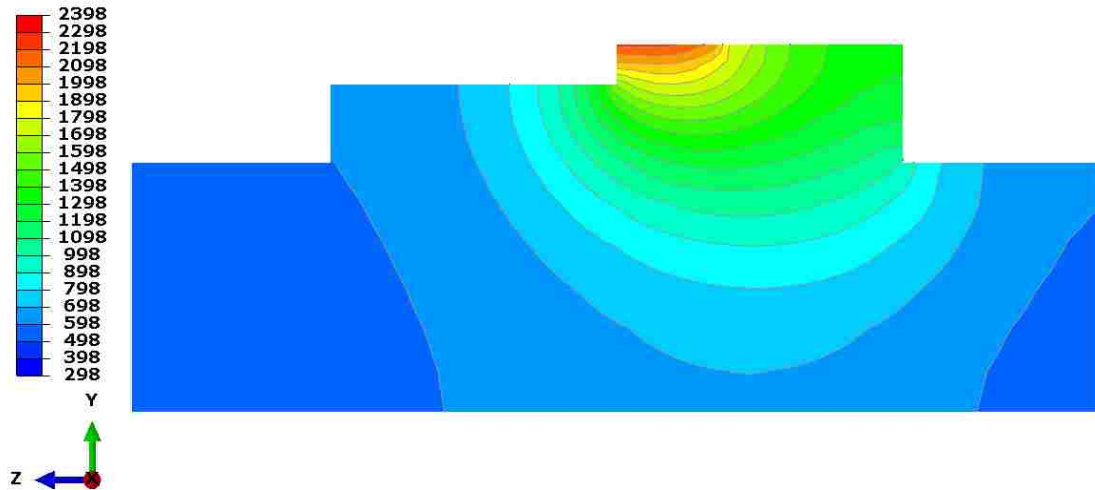
(c)  $t = 4.5$  s

Figure 4.2. Contour Plots of Temperature Field and Isotherms of the Substrate and Deposits from Side View at Different Times (Case 1) (cont.)

Figure 4.3 shows the temperature field of the melt pool and surrounding areas from top view at different times in Case 2 (laser power 910 W, laser travel speed 375 mm/min, powder feed rate 9.4 g/min). Figure 4.4 shows the temperature field and isotherms of the substrate and deposits from side view at different times in Case 2. During the deposition of first layer, the peak temperature during the process was around 2400 K. During the deposition of the second and third layer, the temperature was as high as 2562 K and 2668 K, respectively.

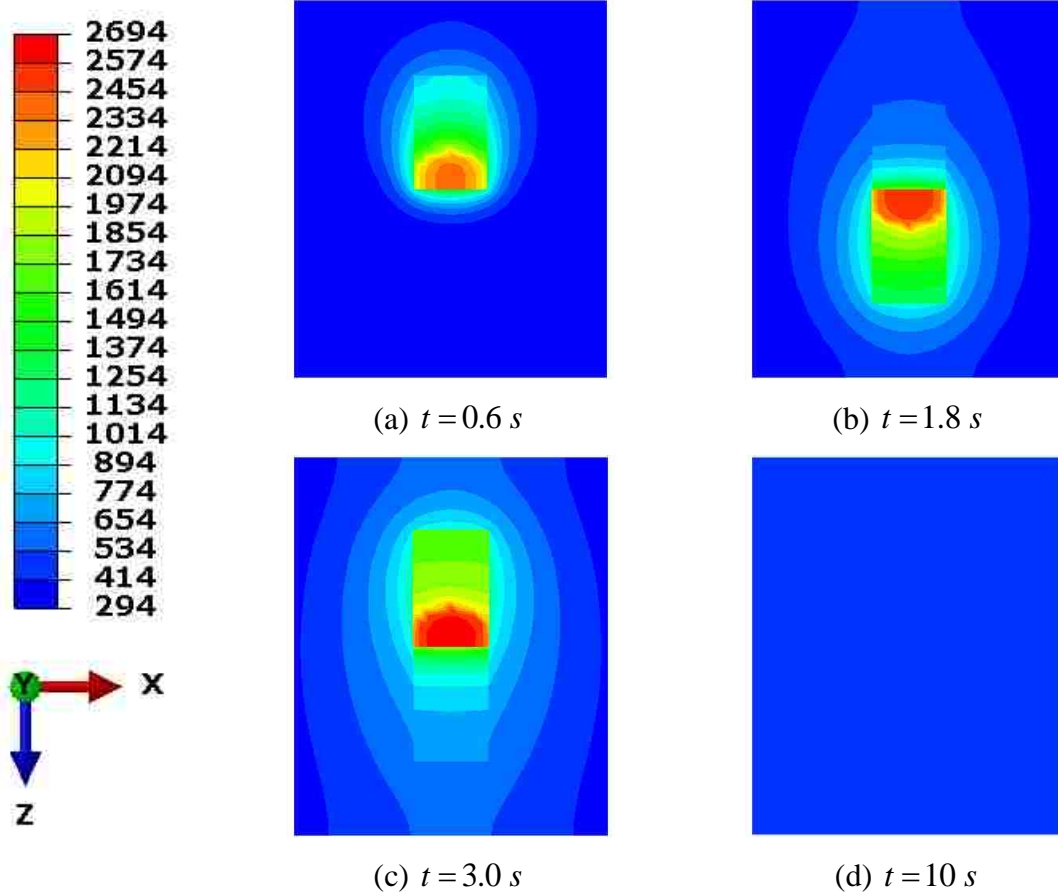
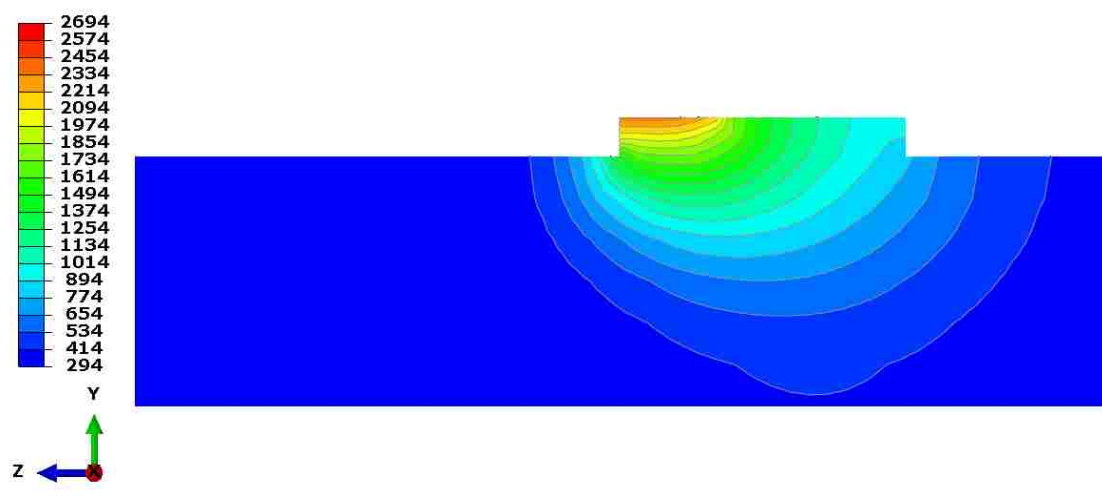
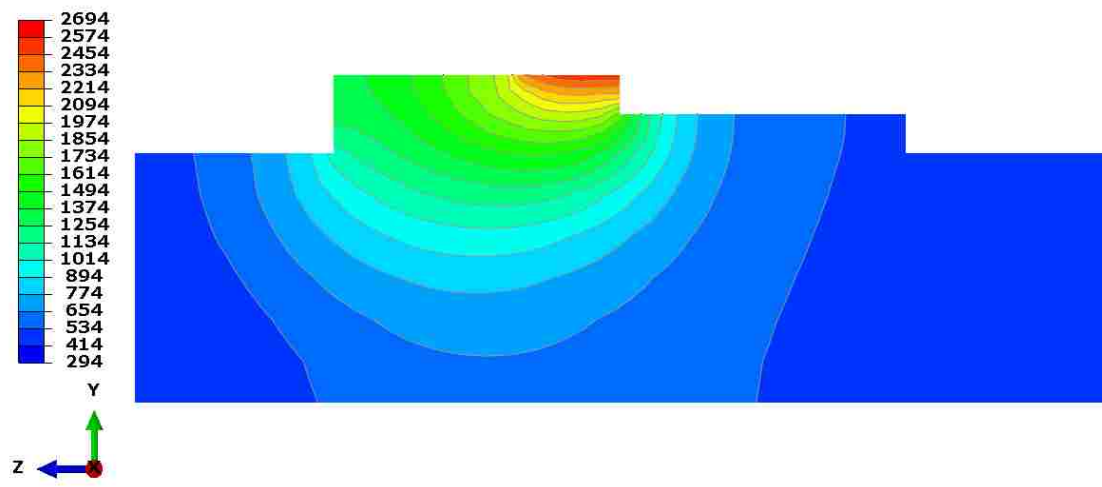


Figure 4.3. Contour Plots of Temperature Field of the Melt pool and Surrounding Areas from Top View at Different Times (Case 2)



(a)  $t = 0.6 s$



(b)  $t = 1.8 s$

Figure 4.4. Contour Plots of Temperature Field and Isotherms of the Substrate and Deposits from Side View at Different Times (Case 2)



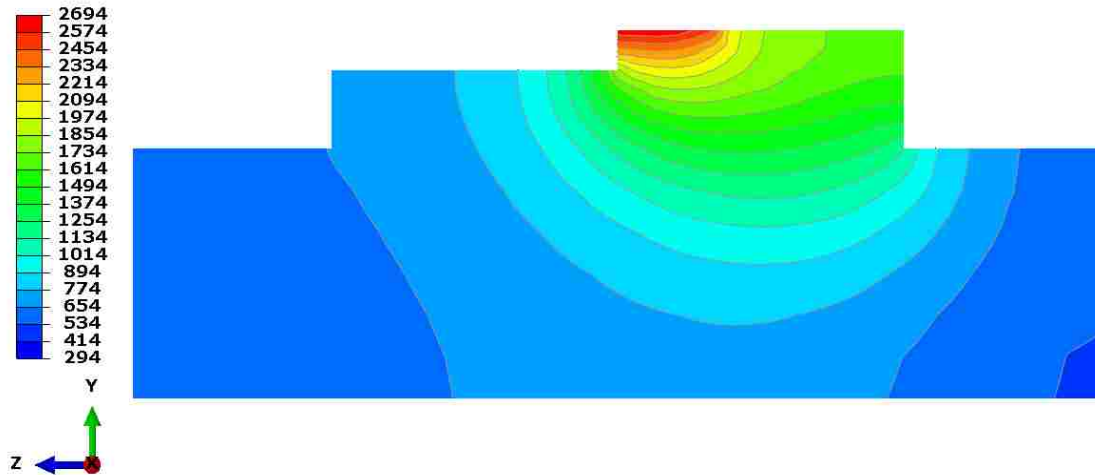
(c)  $t = 3.0 \text{ s}$ 

Figure 4.4. Contour Plots of Temperature Field and Isotherms of the Substrate and Deposits from Side View at Different Times (Case 2) (cont.)

**4.1.2. Temperature Gradient.** The temperature gradient involved in the DMD process was quantitatively analyzed in details. The temperature of nodes along the  $x'$  and  $y'$  (shown in Figure 4.5) axis in simulation Case 1 at  $t = 4.5 \text{ s}$  are shown in Figure 4.6. The  $x'$ -direction nodes were selected along the top surface of the substrate (bottom surface of the deposits), while the  $y'$ -direction nodes were selected along the height of the deposits. The temperature of the substrate's top surface reached a maximum of  $1069 \text{ K}$  just below the center of the laser beam and decreased gradually along the  $x'$  direction. In the  $y'$  direction, the temperature of the deposits reached a maximum of  $2220 \text{ K}$  on the top surface of the deposits and decreased rapidly to  $1069 \text{ K}$ . The slopes of the temperature curves represent the thermal gradients along the  $x'$  and  $y'$  direction. Along  $x'$ , the temperature gradient reached a maximum of  $483 \text{ K/mm}$ ; along  $y'$ , the maximum temperature gradient occurred near the top surface of the deposits, reaching  $1416 \text{ K/mm}$  and then decreasing along the negative  $y'$  direction. These steep thermal gradients induced large compressive strains within the deposits and substrates (Merzelis and Kruth, 2006).

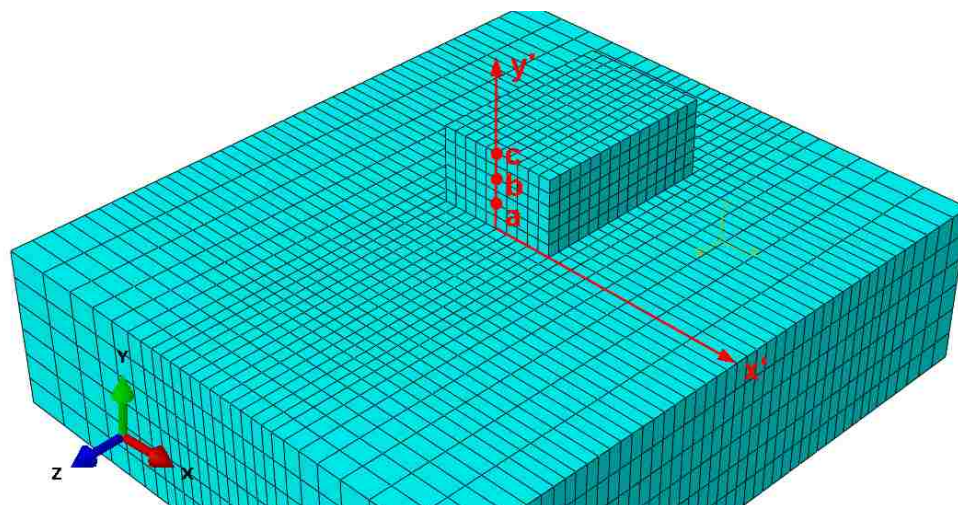


Figure 4.5. Location of Points within Deposition Under Consideration

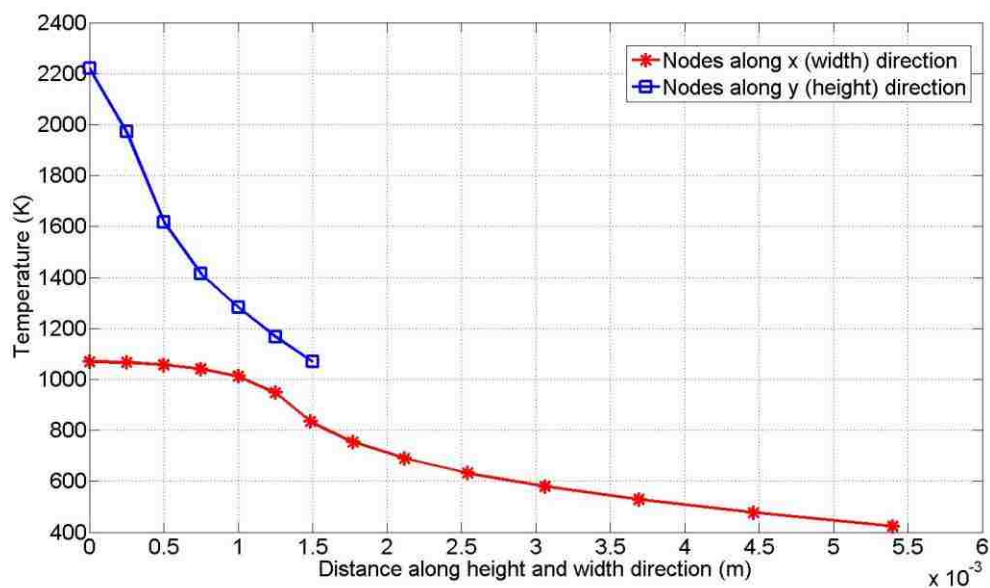


Figure 4.6. Temperature of Nodes in x and y Directions in Case 1 at  $t = 4.5$  s

**4.1.3. Heating and Cooling Rate.** The temperature history of nodes a, b, and c within deposits (shown in Figure 4.5) appears in Figure 4.7. The slopes of the temperature curves represent the heating and cooling rate. Take the temperature history of node a as an example, the temperature was raised from  $298$  K to  $2200$  K in  $0.3$  s and

it dropped again to  $1000\text{ K}$  in about  $0.43\text{ s}$ . Further, as found by taking the derivative of temperature with respect to time at every data point, the heating and cooling rate involved in the DMD process can be as high as  $3000\text{ K/s}$ .

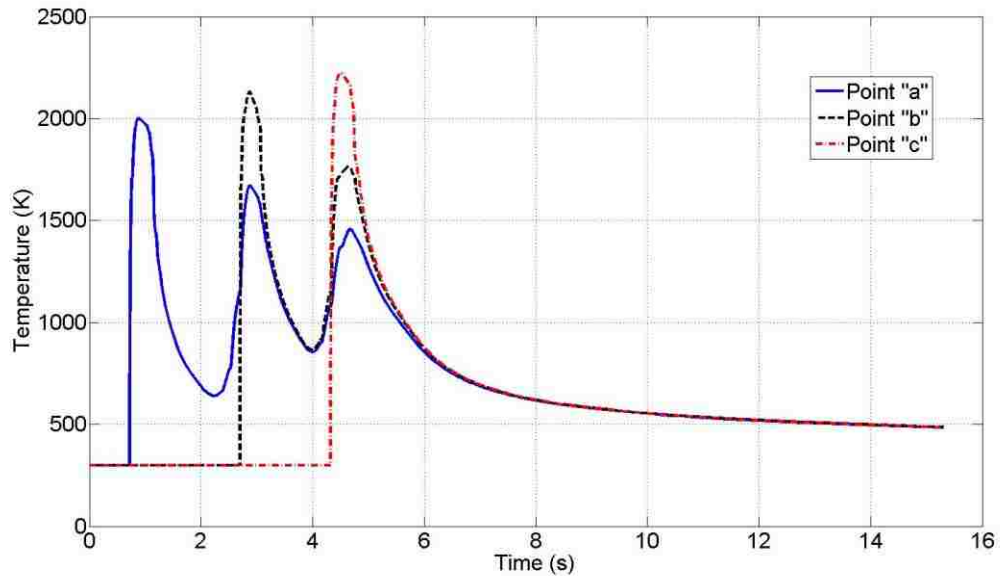


Figure 4.7. Temperature History of Nodes a, b, and c

**4.1.4. Superheat.** During the 3-layer DMD process, the highest temperature for each layer in Case 1 was  $2000\text{ K}$ ,  $2214\text{ K}$ , and  $2350\text{ K}$ , respectively. The liquidus temperature of Stainless Steel 304 is  $1733\text{ K}$ , so large magnitude of superheat would be involved in the DMD process (shown in Figure 4.8). With the constant laser power used in this study, the superheat kept increasing in each layer; however, the rate of the increase tended to decrease.

The superheat is generally not beneficial for the deposition quality, so in the DMD process, high laser power is only used in the beginning of deposition to create the melt pool and then reduce to some value to maintain the melt pool. This process can be accomplished by using a temperature feed-back control system.

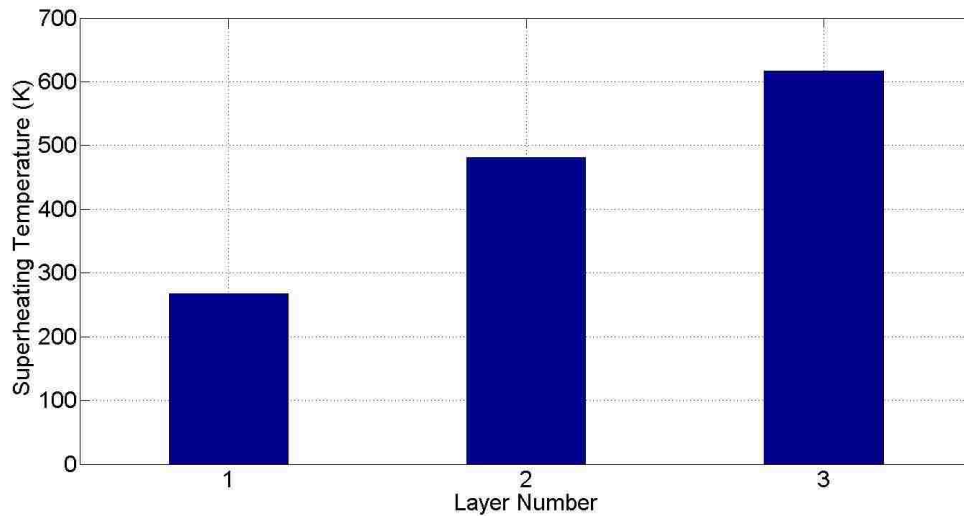


Figure 4.8. Superheating Temperature in Each Deposition Layer in Case 1

#### 4.2. INSTANTANEOUS STRESS

The instantaneous von Mises stress within the deposits during the DMD process is shown in Figure 4.9. As the DMD process started, the von Mises stress rapidly increased to  $360 \text{ MPa}$ ; during the deposition process, it maintained a value between  $265 \text{ MPa}$  and  $360 \text{ MPa}$ ; and after the laser was turned off, it increased again to  $363 \text{ MPa}$ .

The von Mises stress after the deposition process had similar magnitude with that during the deposition process. Considering the fact that the yield stress was significantly reduced by the high temperature involved in the deposition process, crack and fracture would be more likely to happen before the deposition is finished.

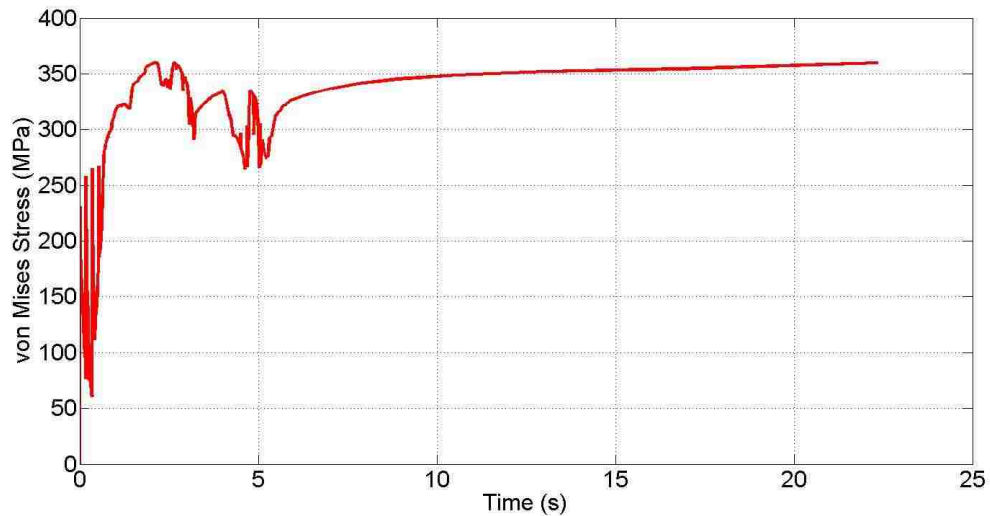


Figure 4.9. Instantaneous von Mises Stress during the DMD Process

### 4.3. RESIDUAL STRESS

The nature and magnitude of residual stresses exist in final deposits would affect the integrity of the entire structure. In general conditions, compressive residual stresses are advantageous since they increase the load resistance and prevent crack growth while tensile residual stresses are detrimental that they reduce the load resistance and accelerate crack growth.

The residual stress distribution within the final deposits is shown in Figure 4.10 and Figure 4.11 (half of the deposits are hidden to show the internal residual stress). Normal stresses  $\sigma_{11}$ ,  $\sigma_{22}$  and  $\sigma_{33}$  along three spatial directions are shown in Figure 4.10-4.11 (a)-(c), respectively, and the von Mises stress is shown in Figure 4.10-4.11 (d). As the figures indicate, residual stresses in the lower part of the deposits were mostly tensile stresses due to the cool-down phase of the molten layers (Merzelis and Kruth, 2006). After the deposition was finished, the remelted lower part of the deposits began to shrink; this shrinkage was restricted by the underlying material, thus inducing tensile stresses. Compressive residual stresses existed at the top free surface of the deposits, caused by the steep temperature gradient. The expansion of the hotter top layer was inhibited by the underlying material, thus introducing compressive stress at the top surface.

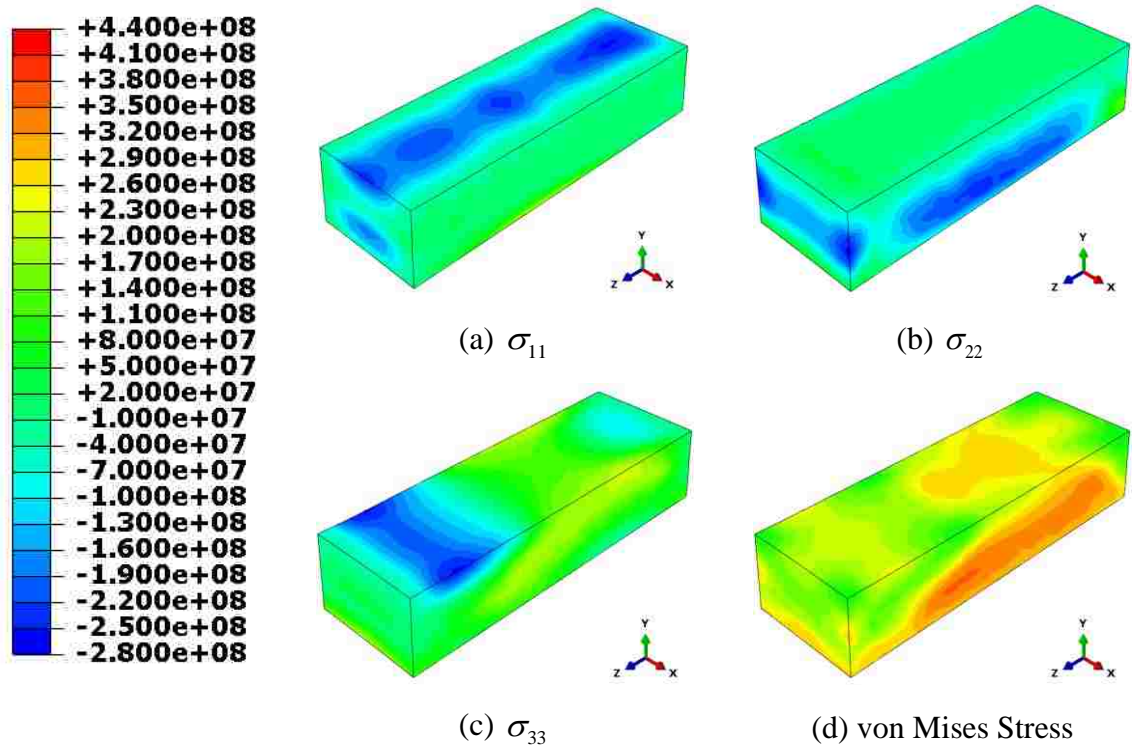


Figure 4.10. Contour Plots of Residual Stress Field within Deposits (exterior faces)



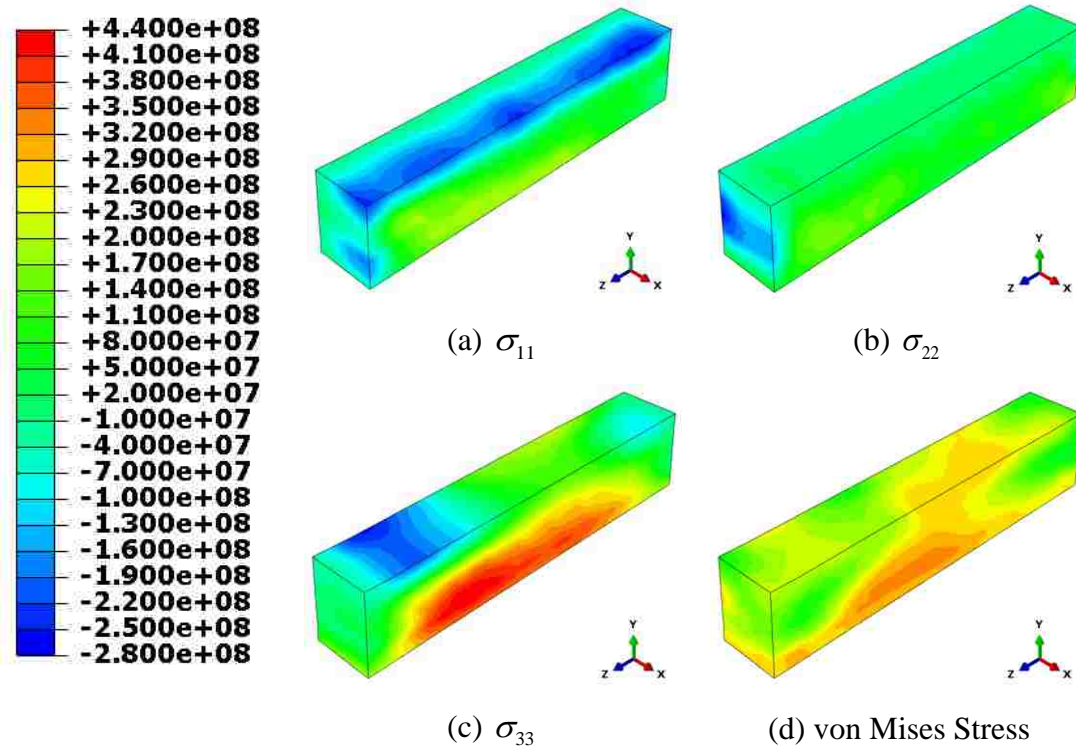
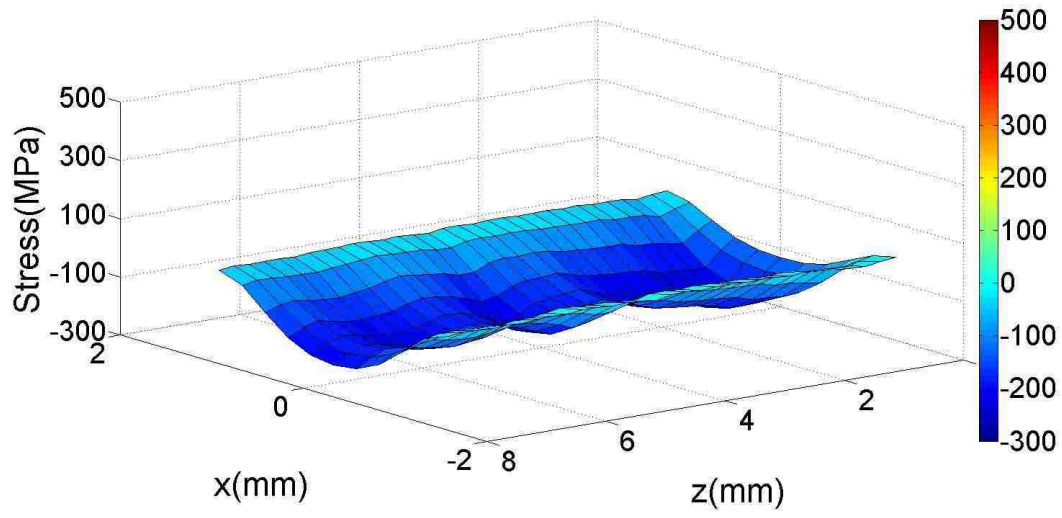
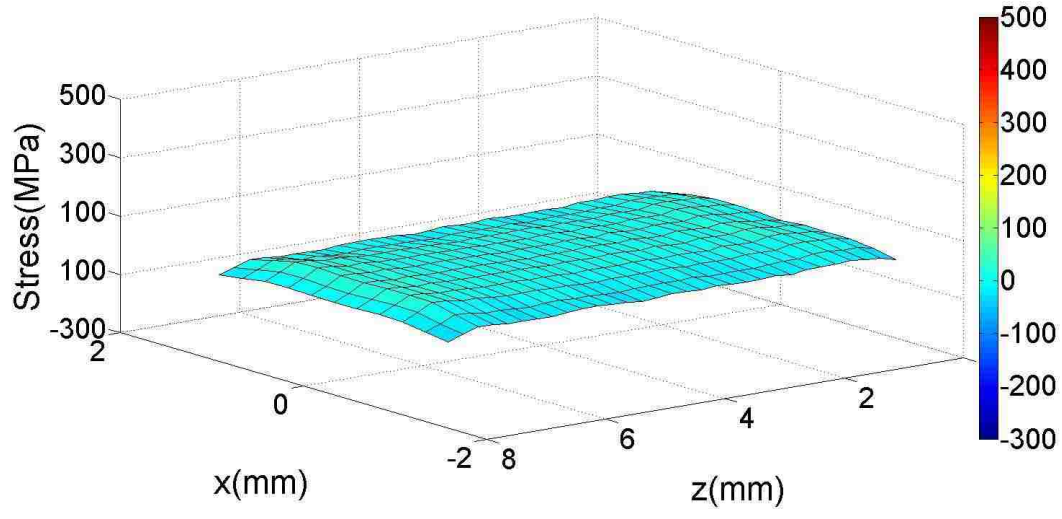


Figure 4.11. Contour Plots of Residual Stress Field within Deposits (y-y cross section)

The distribution and magnitude of residual stresses at the top surface of the deposits are shown in Figure 4.12. Along the x direction, the middle part of the top surface was compressed with a stress magnitude of approximately  $200 \text{ MPa}$ , while the two edges along the z direction were slightly tensioned. Along y, the residual stresses almost vanished. For the normal stresses along z, tensile stresses with a magnitude of approximately  $200 \text{ MPa}$  existed near the center part, and compressive stresses ranging from 0 to  $200 \text{ MPa}$  existed at both ends.



(a)  $\sigma_{11}$  at top surface



(b)  $\sigma_{22}$  at top surface

Figure 4.12. Residual Stress at the Top Surface of Deposits



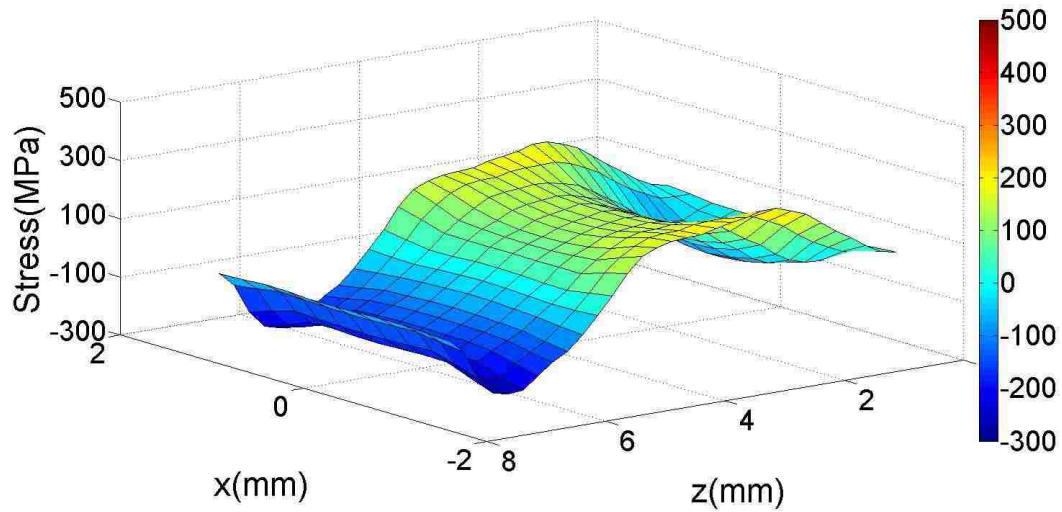
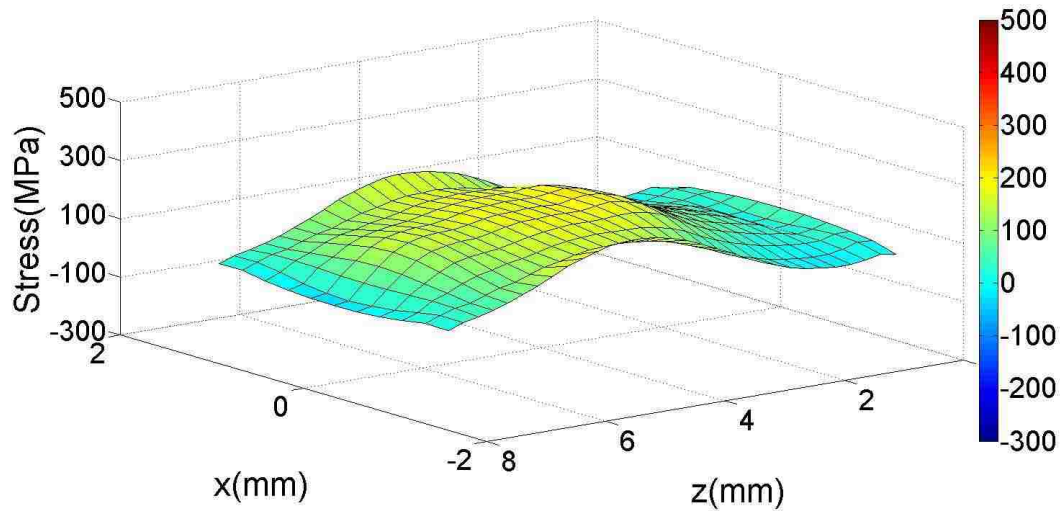
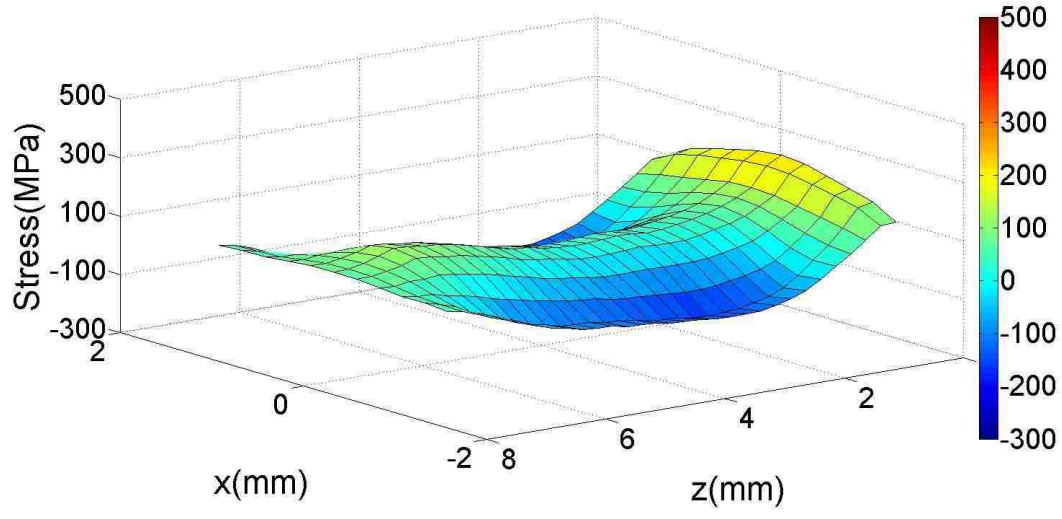
(c)  $\sigma_{33}$  at top surface

Figure 4.12. Residual Stress at the Top Surface of Deposits (cont.)

The distribution and magnitude of residual stresses at the bottom surface of the deposits (also the top surface of the substrate) are shown in Figure 4.13. For the normal stress along  $x$ , the bottom surface was tensioned. The tensile stresses experienced their minimum magnitude at both ends and gradually increased to their maximum value around  $200 \text{ MPa}$  near the center. The normal stress along  $y$  also was tensile stress with a generally low magnitude that increased in both ends. Along  $z$ , tensile stresses with a large magnitude existed;  $\sigma_{33}$  experienced its minimum value of approximately  $200 \text{ MPa}$  at both ends and its maximum value of approximately  $300 \text{ MPa}$  near the center. Since large tensile stresses exist at the bottom surface of deposits, which is the surface connecting the substrate and deposits, crack or fatigue would easily happen here.



(a)  $\sigma_{11}$  at bottom surface



(b)  $\sigma_{22}$  at bottom surface

Figure 4.13. Residual Stress at the Bottom Surface of Deposits

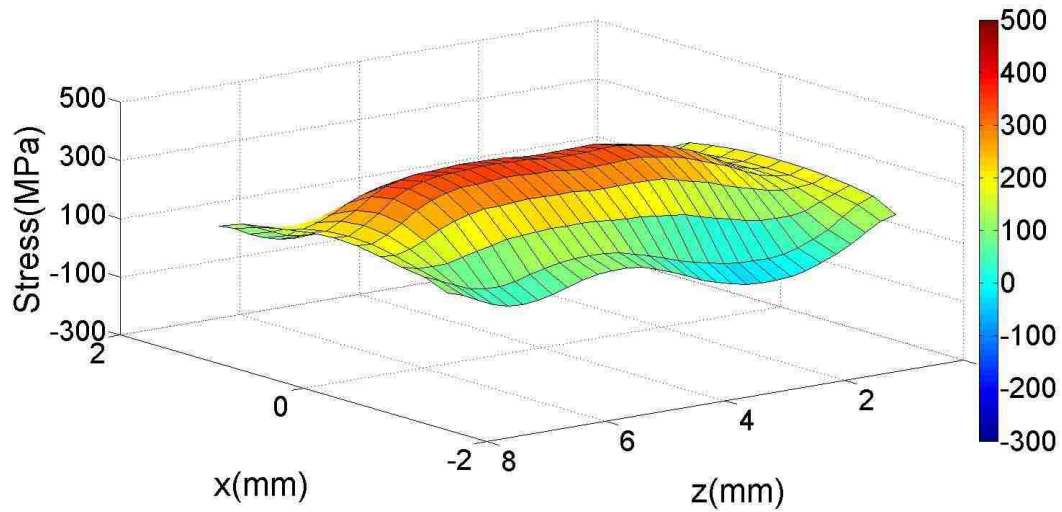
(c)  $\sigma_{33}$  at bottom surface

Figure 4.13. Residual Stress at the Bottom Surface of Deposits (cont.)

Various experimental methods for measuring residual stress have been developed, such as destructive methods, including incremental hole drilling (Casavola et al. 2008), layer removal (Tanaka et al., 2010) and crack compliance (Merzelis and Kruth, 2006), and non-destructive methods including X-ray diffraction (Zheng et al., 2004) and neutron diffraction (Moat et al., 2011, Zaeh and Branner, 2010). These methods could be used to measure the residual stress directly with relatively good accuracy; however, they usually are not cost effective or easy to set up. Therefore, instead of measuring the residual stress directly, a flexible indirect method has been developed for residual stress validation. A one-one relationship exists between the deflection of the substrate and residual stress; therefore, by validating the deflection of the substrate, the residual stress results can be validated indirectly.

#### 4.4. DEFORMATION

During the DMD process, the substrate will continuously expand and shrink, finally maintaining a deformed shape (Figure 4.14). In this study, deflection along y was the main deformation under consideration and is shown in Figure 4.15.



Figure 4.14. Final Shape of Substrate

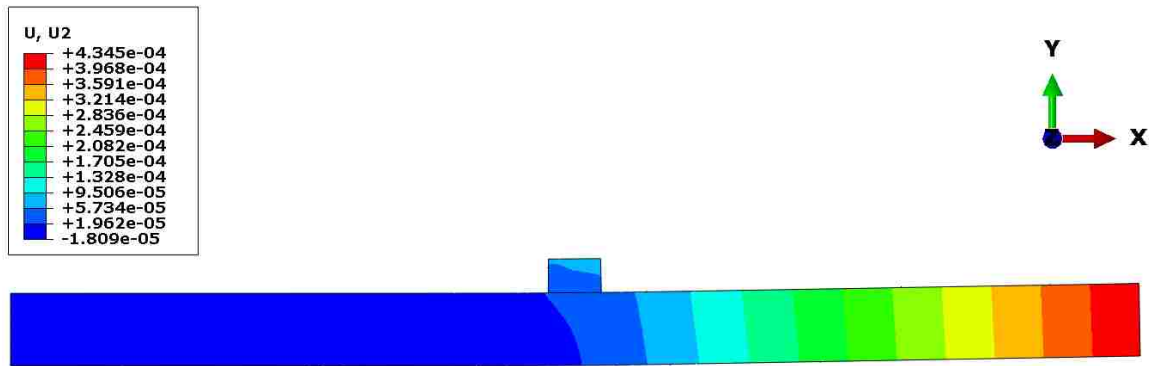


Figure 4.15. Deflection of Substrate along y

**4.4.1. Experiment Setup.** As shown in Figure 4.16, in the experiment, the substrate was clamped at the left end to prevent rigid body motion. Keyence's LK-G5000 series laser displacement sensor shown in Figure 4.17 was placed just below the right end of the substrate to record the displacement of the free end along the y direction with a frequency of 25 Hz during the process. The experimental results appear in Figure 4.18.

The entire DMD process was controlled by the “Laser Aided Material Deposition System” (Liou et al., 2001).

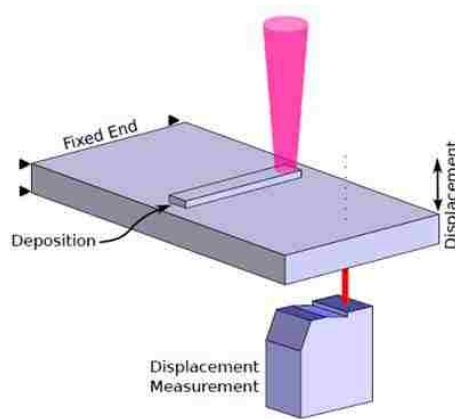


Figure 4.16. Experimental Setup

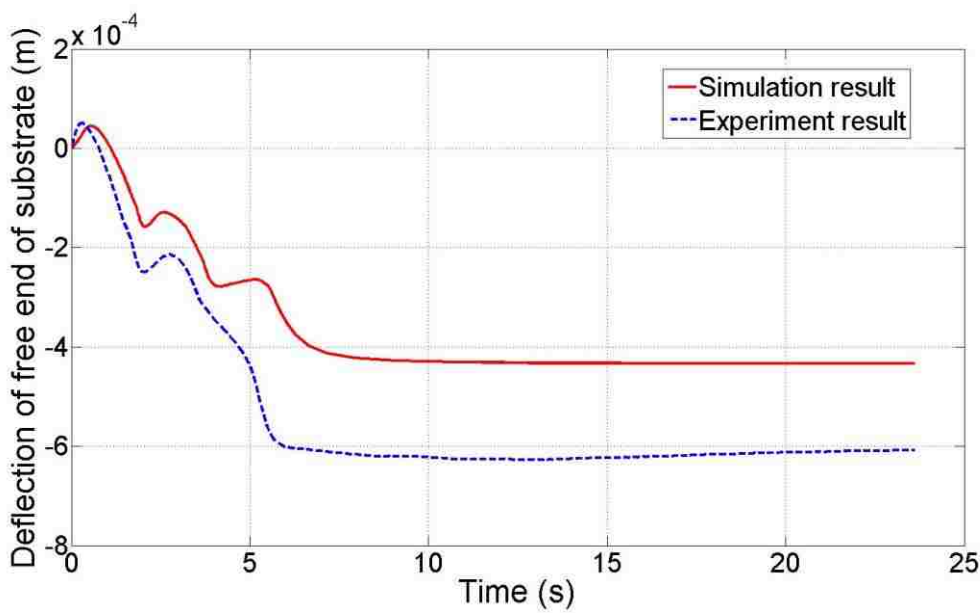


Figure 4.17. Laser Displacement Sensor

**4.4.2. Experimental and Simulation Results.** Figure 4.18 illustrates the comparisons of the substrate deflection between the experimental and simulation results for both cases. These plots indicate that the trend of the deflection calculated from the simulation matched very well with the experimental results. For each deposition layer, the substrate firstly bent down due to thermal expansion on the top surface and then bent up due to thermal shrinkage during the cooling process. After completely cooling down, the substrate maintained its deformed shape.

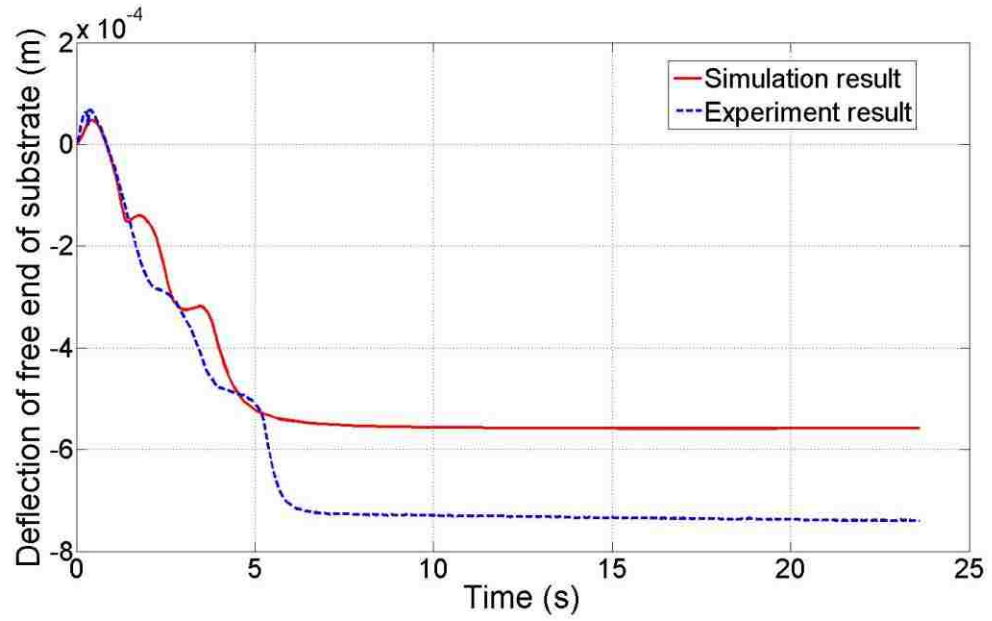
The differences in the final deflection values between the simulation and experiment were 28.5% and 24.6% for Cases 1 and 2, respectively. There are several potential reasons for these differences. Firstly, errors existed in the experimental set-up. In the simulation, the laser beam traveled exactly along the centerline of the substrate. However, this cannot be perfectly accomplished in experiments (Figure 4.14). These offsets would affect the deflection to a large extent because the deflection is sensitive to the positions of heated zone and measuring point (where expansion and shrinkage mainly happens). Secondly, the laser displacement sensor did not track the displacement of one particular node. It works by sensing the signal reflected by an obstacle, so the positions it

monitors are always changing as the substrate continuing to deform. The simplifications and assumptions considered in both thermal and mechanical analysis are also important factors contributing to the differences between the simulation and experiment.



(a) Deflection in Case 1

Figure 4.18. Simulation and Experimental Results of Substrate Deflection



(b) Deflection in Case 2

Figure 4.18. Simulation and Experimental Results of Substrate Deflection (cont.)

## 5. DISCUSSION

The simulation results of temperature field are influenced by process parameters, material properties, and boundary conditions. For process parameters, both laser power and laser traveling speed have significant effect on the temperature field. Among material properties, the thermal conductivity has some effect on the temperature field while the effect of material density and specific heat on temperature field can be neglected. The transient temperature distribution is sensitive to boundary conditions including convection and radiation, thus it is important to apply accurate, temperature-dependent thermo-physical properties such as convection coefficient and emissivity in the model in order to obtain realistic results. In addition, the forced convection caused by the shielding gas is also an important factor which will result in a faster cooling rate of melt pool.

Among the mechanical material properties, the yield stress has the most significant effect on the residual stress and deformation. When the temperature increases, the yield stress decreases rapidly, inducing plastic strains. The elastic properties including Young's modulus and the thermal expansion coefficient have small effects on the residual stress and deformation. Several approaches can be applied to reduce the residual stress. By reducing the cooling rate, pre-heating of the substrate and post-scanning of the deposited materials can reduce the residual stress to a large extent. The residual stress also can be relieved by heat treatment after deposition. In addition, laser scanning strategy is an important factor would affect the residual stress-scanning along the width of the substrate would produce larger residual stress than scanning along the length of the substrate.

One of the major challenges involved in numerical simulation is the computation time. The approaches utilized in this thesis to reduce the computation time are to use the combined boundary condition and meshes with different sizes and orders. For more complicated deposition patterns and geometries, adaptive meshes can be applied to greatly reduce the computation cost.

The material considered in this thesis is Stainless Steel 304, so the results cannot be simply extrapolated to other materials such as carbon steel and titanium alloy. During the DMD process of carbon steel and titanium alloy, phase transformation would greatly



affect the residual stress and final deformation. Governing equations describing the strain due to the volumetric change in the phase transformation and strain caused by transformation plasticity must be considered.

By further combining the temperature field together with cellular automaton method, the solidification microstructure evolution, including grain size and shape information, can also be simulated.

## **6. CONCLUSION AND SCOPE OF FUTURE WORK**

### **6.1. CONCLUDING REMARKS**

To investigate the features of thermal and mechanical behavior of deposited materials involved in the DMD process, a sequentially coupled, thermo-mechanical finite element model was developed for multi-layer DMD process of Stainless Steel 304. The results revealed the characteristics of temperature distribution, residual stress and deformation within the formed deposits and substrates. A set of experiments were conducted to validate the mechanical effects using a laser displacement sensor. This FEA model can be used to predict the mechanical behavior of products fabricated by the DMD process or similar processes with localized heat sources such as laser sintering, laser cladding and welding.

### **6.2. SCOPE OF FUTURE WORK**

The following issues need to be discussed and incorporated in the proposed simulation program for DMD process.

1. The geometry of the deposited materials is assumed to be rectangular blocks in in the present model; however, during the real DMD process, it is formed into some certain shape. Thus the geometry of the deposited materials must be predicted in future models.
2. The proposed model needs to be verified for the temperature distribution and stress/strain by experimental means.
3. The present model simulates the DMD process for straight pass only. More complicated situations including various tool paths and geometry should also be considered in the future.
4. The present model assumes a continuous wave (CW) laser beam. It would be desirable to include pulsed laser in the program as well.
5. In the present model, constant laser power and traveling speed is considered. For laser deposition system with feed-back control system, time dependent laser power and traveling speed should be considered.

6. Different process parameters including laser power, laser travel speed, powder feed rate and deposition pattern need further discussion order to control the residual stress and final deformation.

APPENDIX A  
SUBROUTINE TO SIMULATE THE MOVING HEAT SOURCE

The following FORTRAN user subroutine in ABAQUS is written according to Equation (6) to simulate the movement of laser beam and to calculate the heat flux goes into the substrate and deposits.

```

SUBROUTINE DFLUX(FLUX,SOL,KSTEP,KINC,TIME,NOEL,NPT,COORDS,
1 JLTYP,TEMP,PRESS,SNAME)
INCLUDE 'ABA_PARAM.INC'

DIMENSION FLUX(2),TIME(2),COORDS(3)
CHARACTER*80 SNAME

V=0.25/60           ! Travel speed is 250 mm/min
RBEAM=0.00125      ! Radius of laser beam
VI=607.0           ! Laser power
EFF=0.4            ! Absorptivity of the substrate and powder
QTOT=EFF*VI        ! Equivalent laser power
Q=QTOT/(3.1415*(RBEAM**2.0))  % Power density

C  Deactivate the powder element (Model Change)
  if(TIME(2).LE.0.00000001)THEN
    ZM=0
    XM=COORDS(1)

C  First layer
  ELSE IF(TIME(2).GE.0.00000001.AND.TIME(2).LE.1.80000011)THEN
    ZM=COORDS(3)-V*(TIME(2)-0.00000001)-0.0026
    XM=COORDS(1)

C  Second layer
  ELSE IF(TIME(2).GE.1.80000012.AND.TIME(2).LE.3.60000022)THEN
    ZM=COORDS(3)+V*(TIME(2)-1.80000011)-0.0026-0.0075

```

```
XM=COORDS(1)
ELSE

C  Third layer
ZM=COORDS(3)-V*(TIME(2)-3.60000022)-0.0026
XM=COORDS(1)
END IF

C  Heat flux only exists within the laser beam; in areas outside of the laser beam, the
heat C flux is 0
R=SQRT(ZM**2.0+XM**2.0)
C=(R**2.0)/(RBEAM**2.0)
IF(C.GT.1.0) GOTO 10

FLUX(1)=Q
10 RETURN
20 CONTINUE
END
```

APPENDIX B

SUBROUTINE TO SIMULATE THE COMBINED BOUNDARY CONDITION

The following FORTRAN user subroutine in ABAQUS is written according to Equation (10) to consider the combined convection and radiation effect.

```
SUBROUTINE FILM(H,SINK,TEMP,KSTEP,KINC,TIME,NOEL,NPT,  
1 COORDS, JLTYP, FIELD, NFIELD, SNAME, NODE, AREA)  
  INCLUDE 'ABA_PARAM.INC'  
  DIMENSION H(2), TIME(2), COORDS(3), FIELD(NFIELD)  
  CHARACTER*80 SNAME  
  
  SINK=298.15                ! Sink temperature  
  H(1)=0.002169*(TEMP**1.61) ! Film coefficient  
  H(2)=0.0034921*(TEMP**0.61) ! Rate of change of the film coefficient  
30 RETURN  
40 CONTINUE  
  END
```



APPENDIX C  
TEMPERATURE-DEPENDENT THERMAL PROPERTIES OF AISI 304 STAINLESS  
STEEL

Temperature (K)	Density (Kg/m <sup>3</sup> )	Specific heat (J/Kg · K)	Conductivity (W/m · K)
300	7894	510.03	12.97
400	7860	523.42	14.59
500	7823	536.81	16.21
600	7783	550.20	17.82
700	7742	564.00	19.44
800	7698	577.39	21.06
900	7652	590.78	22.68
1000	7603	604.17	24.30
1100	7552	617.56	25.91
1200	7499	631.37	27.53
1300	7444	644.75	29.15
1400	7386	658.14	30.77
1500	7326	671.53	32.39
1600	7264	685.34	34.00
1703	7197	698.73	35.67
1733	6905	794.96	17.92
1800	6862	794.96	18.14
1900	6795	794.96	18.46
2000	6725	794.96	18.79
2100	6652	794.96	19.11
2200	6576	794.96	19.44
2300	6498	794.96	19.76
2400	6416	794.96	20.09
2500	6331	794.96	20.41
2600	6243	794.96	20.73
2700	6152	794.96	21.06
2800	6058	794.96	21.38

APPENDIX D  
TEMPERATURE-DEPENDENT MECHANICAL PROPERTIES OF AISI 304  
STAINLESS STEEL

### Temperature-Dependent Thermal Expansion Coefficient of SS 304

Temperature (K)	Thermal Expansion Coefficient (1/K)
400	1.468
500	1.524
600	1.581
700	1.639
800	1.699
900	1.759
1000	1.821
1100	1.885
1200	1.949
1300	2.016
1400	2.084
1500	2.154
1600	2.225
1700	2.299

### Temperature-Dependent Young's Modulus and Poisson's Ratio of SS 304

Temperature (K)	Young's Modulus (GPa)	Poisson's ratio
273.15	198.5	0.294
373.15	193.0	0.295
473.15	185.0	0.301
573.15	176.0	0.31
673.15	167.0	0.318
873.15	159.0	0.326
1073.15	151.0	0.333
1473.15	60.0	0.339
1573.15	20.0	0.342
1773.15	10	0.388

### Temperature-Dependent Plastic Stress/Strain Variation for AISI 304 Stainless Steel

Temperature (K)	Plastic Strain	Yield Stress (MPa)
297	0	254
297	0.1	444
366	0	211
366	0.1	401
477	0	176
477	0.1	366
589	0	155
589	0.1	345
700	0	143
700	0.1	333
811	0	132
811	0.1	322
922	0	119
922	0.1	309
977	0	112
977	0.1	301
1023	0	102
1023	0.1	262
1073	0	84
1073	0.1	194
1123	0	62
1123	0.1	112
1173	0	40
1173	0.1	41
1273	0	15
1273	0.1	15
1373	0	6
1373	0.1	6

1473	0	3
1473	0.1	3
1700	0	1
1700	0.1	1

## BIBLIOGRAPHY

- Aggarangsi, P., Beuth, J. L. and Griffith, M. (2003) "Melt pool size and stress control for laser-based deposition near a free edge" in *14th Solid Freeform Fabrication Proceedings*, Austin, Texas USA. pp. 196-207.
- Alimardani, M., Toyserkani, E. and Huissoon, J. P. (2007), "A 3D dynamic numerical approach for temperature and thermal stress distributions in multilayer laser solid freeform fabrication process". *Optics and Lasers in Engineering*, Vol. 45 No. 12, pp. 1115-1130.
- Casavola, C., Campanelli, S. and Pappalettere, C. (2008) "Experimental analysis of residual stresses in the selective laser melting process" in *Proceedings of 2008 SEM International Conference and Exposition on Experimental and Applied Mechanics*, Orlando, Florida USA.
- Chakrabarty, J. (2006), *Theory of plasticity*, Butterworth-Heinemann, Boston, MA.
- Deng, D. (2009), "FEM prediction of welding residual stress and distortion in carbon steel considering phase transformation effects". *Materials & Design*, Vol. 30 No. 2, pp. 359-366.
- Deng, D. and Murakawa, H. (2006), "Numerical simulation of temperature field and residual stress in multi-pass welds in stainless steel pipe and comparison with experimental measurements". *Computational Materials Science*, Vol. 37 No. 3, pp. 269-277.
- Feli, S., Aalami Aaleagha, M., Foroutan, M. and Borzabadi Farahani, E. (2012), "Finite Element Simulation of Welding Sequences Effect on Residual Stresses in Multipass Butt-Welded Stainless Steel Pipes". *Journal of pressure vessel technology*, Vol. 134 No. 1, pp. 441-451.
- Gery, D., Long, H. and Maropoulos, P. (2005), "Effects of welding speed, energy input and heat source distribution on temperature variations in butt joint welding". *Journal of Materials Processing Technology*, Vol. 167 No. 2, pp. 393-401.
- Ghosh, S. (2006) "*Process Modeling for Solidification Microstructure and Transient Thermal Stresses in Laser Aided DMD Process*" Unpublished Doctor of Philosophy, University of Missouri--Rolla.
- Griffith, M., Schlienger, M., Harwell, L., Oliver, M., Baldwin, M., Ensz, M., Essien, M., Brooks, J., Robino, C., JE, S. and et al. (1999), "Understanding thermal behavior in the LENS process". *Materials & Design*, Vol. 20 No. 2, pp. 107-113.

- Kamara, A., Marimuthu, S. and Li, L. (2011), "A numerical investigation into residual stress characteristics in laser deposited multiple layer waspaloy parts". *Transactions of the ASME-B-Journ Manufacturing Science Engineering*, Vol. 133 No. 3, pp. 031013.1-031013.9.
- Kim, C. S. (1975) *Thermophysical properties of stainless steels*: Argonne National Lab., Ill.(USA).
- Kim, J.-D. and Peng, Y. (2000), "Time-dependent FEM simulation of dilution control of laser cladding by adaptive mesh method". *KSME International Journal*, Vol. 14 No. 2, pp. 177-187.
- Labudovic, M., Hu, D., & Kovacevic, R. (2003). A three dimensional model for direct laser metal powder deposition and rapid prototyping. *Journal of materials science*, 38(1), 35-49.
- Lampa, C., Kaplan, A. F., Powell, J. and Magnusson, C. (1997), "An analytical thermodynamic model of laser welding". *Journal of Physics D: Applied Physics*, Vol. 30 No. 9, pp. 1293-1299.
- Liou, F. W., Choi, J., Landers, R., Janardhan, V., Balakrishnan, S. and Agarwal, S. (2001) "Research and development of a hybrid rapid manufacturing process" in *12th Annual Solid Freeform Fabrication Symposium*, Austin, Texas USA. pp. 138-145.
- Long, R., Liu, W. and Shang, X. (2006), "Numerical simulation of transient temperature field for laser direct metal shaping". in Wang, K., Kovacs, G. L., Wozny, M. and Fang, M., (eds.), *Knowledge Enterprise: Intelligent Strategies in Product Design, Manufacturing, and Management*, Springer, Shanghai, China, pp. 786-796.
- Masubuchi, K. (1980). *Analysis of welded structures: Residual stresses, distortion, and their consequences*. Oxford, United Kingdom: Pergamon press.
- Mercelis, P. and Kruth, J.-P. (2006), "Residual stresses in selective laser sintering and selective laser melting". *Rapid Prototyping Journal*, Vol. 12 No. 5, pp. 254-265.
- Moat, R., Pinkerton, A., Li, L., Withers, P. and Preuss, M. (2011), "Residual stresses in laser direct metal deposited Waspaloy". *Materials Science and Engineering: A*, Vol. 528 No. 6, pp. 2288-2298.
- Reddy, J. N. and Gartling, D. K. (2010), *The finite element method in heat transfer and fluid dynamics*, CRC Press LLC, Boca Raton, FL.
- Simulia, D. (2011) ABAQUS 6.11 Analysis User's Manual. in. pp. 22-2.



- Tanaka, R., Hosokawa, A., Ueda, T., Furumoto, T., Aziz, A. and Sanusi, M. (2010), "Study on reduction of residual stress induced during rapid tooling process: Influence of heating conditions on residual stress". *Key Engineering Materials*, Vol. 447 No. 785-789.
- Toyserkani, E., Khajepour, A. and Corbin, S. (2004), "3-D finite element modeling of laser cladding by powder injection: Effects of laser pulse shaping on the process". *Optics and Lasers in Engineering*, Vol. 41 No. 6, pp. 849-867.
- Vinokurov, V. A. (1977), "*Welding Stresses and Distortion: Determination and Elimination*" British Library Lending Division.
- Wang, L. and Felicelli, S. D. (2006), "Analysis of thermal phenomena in LENS™ deposition". *Materials Science and Engineering: A*, Vol. 435 No. 625-631.
- Wang, L., Felicelli, S. D., and Pratt, P. (2008), "Residual stresses in LENS-deposited AISI 410 stainless steel plates". *Materials Science and Engineering: A*, 496(1), 234-241.
- Zaeh, M. F. and Branner, G. (2010), "Investigations on residual stresses and deformations in selective laser melting". *Production Engineering*, Vol. 4 No. 1, pp. 35-45.
- Zheng, X., Li, J. and Zhou, Y. (2004), "X-ray diffraction measurement of residual stress in PZT thin films prepared by pulsed laser deposition". *Acta Materialia*, Vol. 52 No. 11, pp. 3313-3322.
- Zhu, X. and Chao, Y. (2002), "Effects of temperature-dependent material properties on welding simulation". *Computers & Structures*, Vol. 80 No. 11, pp. 967-976.

## VITA

Heng Liu was born in Taixing, Jiangsu, China. He received his Bachelor of Engineering (B.E) in Mechanical Engineering from Southwest Jiaotong University, Chengdu, Sichuan, China in 2011. He has been pursuing his graduate studies in the Department of Mechanical and Aerospace Engineering at the Missouri University of Science and Technology (Formerly University of Missouri - Rolla) since January 2012. During his stay at Missouri S&T, he held position of Graduate Research Assistant. He received his Master of Science degree in Manufacturing Engineering from Missouri University of Science and Technology, Rolla, Missouri, USA in May 2014.

